



OXFORD-UMAT: An efficient and versatile crystal plasticity framework

Eralp Demir ^{a,*}, Alvaro Martinez-Pechero ^a, Chris Hardie ^b, Edmund Tarleton ^a

^a Department of Engineering Science, University of Oxford, Parks road, Oxford OX1 3PJ, UK

^b UK Atomic Energy Authority, Culham Science Centre, Abingdon, Oxfordshire, OX14 3DB, UK

ARTICLE INFO

Dataset link: <https://github.com/TarletonGroup/CrystalPlasticity>

Keywords:

Crystal plasticity
Finite element method
Abaqus UMAT
Time integration methods
Explicit - semi-implicit - fully-implicit state update
Forward-gradient method

ABSTRACT

The crystal plasticity-based finite element method is widely used, as it allows complex microstructures to be simulated and allows direct comparison with experiments. This paper presents the OXFORD-UMAT for Abaqus[®], a novel crystal plasticity code that is publicly available online for researchers interested in using crystal plasticity. The model is able to simulate a wide range of materials and incorporates two different solvers based on the solution of slip increments and Cauchy stress, with variants of state update procedures including explicit, semi-implicit, and fully-implicit for computational efficiency that can be set by the user. Constitutive laws are available for a range of materials with single or multiple phases for slip, creep, strain hardening, and back stress. The model includes geometrically necessary dislocations that can be computed using finite element interpolation functions by four alternative methods, including the total form with and without a correction for the dislocation flux, a widely used rate form, and a slip-gradient formulation. In addition, the initial strengthening and subsequent softening seen in irradiated materials can also be simulated with the model. The analysis is available in 2D (plane stress and plane strain) and 3D, including linear and quadratic elements. Here we include full derivations of the key equations used in the code and then demonstrate the capability of the code by modeling single-crystal and large-scale polycrystal cases. Comparison of OXFORD-UMAT with other available crystal plasticity codes for Abaqus[®] reveals the efficiency of the proposed approach, with the backup solver offering greater versatility for handling convergence issues commonly found in practical applications.

1. Introduction

For the last two decades, crystal plasticity (CP) has been utilized to model materials by integrating the microstructure along with elastic and plastic anisotropy. CP offers the advantage of using various material laws, from phenomenological power-law-based rate-dependent viscoplasticity (Dawson, 2000) to more physically based constitutive laws such as the Orowan equation (Roters et al., 2000). As microstructure sensitivity becomes increasingly crucial in industries such as nuclear, fusion energy, and aerospace, and with advancements in computational efficiency, CP has become a viable option for incorporating anisotropy into material models. Despite its usefulness, the method still encounters difficulties with numerical convergence due to its inherent nonlinear characteristics.

A CP model seeks the solution for the elastic or plastic part of the deformation similar to isotropic plasticity (Weber and Anand, 1990) with an anisotropic plastic flow direction (Busso and Cailletaud, 2005). For this reason, the total deformation is multiplicatively decomposed into its elastic and plastic parts for the most generalized case of large deformation (Lee, 1969). Plastic deformation possesses the unique

property of slip that does not alter the lattice orientation while conserving volume. Various solution methods have been developed to formulate the CP problems based on different variables such as: Cauchy stress (Asaro and Needleman, 1985), slip increments (Huang, 1991), 2nd Piola-Kirchoff stress (Kalidindi et al., 1992), plastic part of the deformation (Maniatty et al., 1992), elastic part of the deformation gradient (Sarma and Zacharia, 1999), volumetric/deviatoric part of the stress (Marin and Dawson, 1998) and plastic velocity gradient (Roters et al., 2012).

Crystal plasticity-based solvers have been implemented in various computational frameworks, including finite elements (Roters et al., 2012, 2019), spectral (Lebensohn, 2001; Knezevic et al., 2016), and more recently in peridynamics (Sun and Sundararaghavan, 2014; Gu et al., 2019) to predict the mechanical response of polycrystals on grain scales. All aim to incorporate more physics into the models while considering the microstructural anisotropy. The crystal plasticity-based finite element method (CPFEM) ensures local fulfillment of compatibility and mechanical equilibrium, thus offering a more accurate solution than the Schmid, Taylor, or Self-Consistent homogenization

* Corresponding author.

E-mail address: eralp.demir@eng.ox.ac.uk (E. Demir).

Nomenclature	
F	mechanical deformation gradient
\dot{F}	time rate of change of mechanical deformation gradient
F_e	elastic part of the deformation gradient
F_p	plastic part of the deformation gradient
F_{tot}	total deformation gradient
L	velocity gradient
L_e, L_p	elastic and plastic velocity gradients
F_θ	thermal part of the deformation gradient
$\theta, \Delta\theta$	temperature and its increment
$\Delta E_\theta^c, \Delta E_\theta$	thermal strain increments in the crystal and sample reference
g	current crystal to sample transformation
g_0	initial crystal to sample transformation
G	special crystal to sample transformation matrix for elasticity in direct notation
σ	Cauchy stress rate
Ω	anti-symmetric spin
Ω_e, Ω_p	elastic and plastic parts of spin tensor
D	symmetric total stretch rate
D_e, D_p	elastic and plastic stretch rates
P^a	plastic stretch tensor for slip system a
W^a	plastic spin tensor for slip system a
I	2nd order identity tensor (matrix)
Δt	time increment
α	thermal expansion matrix
α	geometric factor in Taylor's strength
$\alpha_1, \alpha_2, \alpha_3$	thermal expansion coefficients of the lattice in three directions
ψ	stress residual
σ	Cauchy stress
∇	Jaumann stress rate with respect to the reference frame attached to the crystal lattice
σ_{tr}	trial stress
ϕ	weight of fully plastic stress guess in the initial stress guess
$\Delta \epsilon$	total strain increment
$\Delta \epsilon_e, \Delta \epsilon_p$	elastic and plastic strain increments
$\Delta \sigma$	stress increment
f	fraction of mean CRSS to set the stress increments during iteration
Ψ	slip increment residual
ϑ	implicit time integration parameter
ξ^a	slip residual in forward-gradient method
N_b^a	coefficient in forward-gradient method
δ_b^a	Kronecker delta for slip systems
τ^a	resolved shear stress (RSS)
τ_c^a	critical resolved shear stress (CRSS)
τ_{cef}^a	effective CRSS
τ_c^0	lattice friction
$\bar{\tau}_c$	average CRSS over slip systems
$\dot{\gamma}^a, \Delta \dot{\gamma}^a$	slip rate and its increment in slip system a
γ^a	total slip rate in slip system a
Γ	cumulative slip
A^a, B^a	parameters for hyperbolic-sine slip law
b^a	Burgers vector in slip system a
ΔF	Helmholtz free energy
ΔV^a	activation volume in slip system a
ϱ_m, ϱ_m^0	mobile dislocation density and its reference value
ΔV_0	activation volume scaling factor
λ^a	jump distance
v_0	dislocation vibration frequency
k_B	lattice Boltzmann constant
n	rate-sensitivity exponent
$\dot{\gamma}_0$	reference slip rate
p, q	constants characterizing the shape of the statistical obstacle profile
$\dot{\gamma}_C, \dot{\gamma}_D$	reference creep and damage rates
b_C, b_D	creep and damage stress multipliers
Q_C, Q_D	activation energies for creep and damage
R	universal gas constant
$Y^a, \dot{Y}^a, \Delta Y^a$	a general state variable, its evolution rate, and its increment in slip system a
ϱ_{for}^a	forest dislocation density in slip system a
$\varrho_{SSD}^a, \dot{\varrho}_{SSD}^a$	statistically-stored dislocation density and its evolution rate in slip system a
χ	Mapping from SSD to screw and edge dislocations
$\varrho_{SSDe}^a, \varrho_{SSDs}^a$	edge and screw types SSD density in slip system a
ϱ_{GND}^a	geometrically necessary dislocation density in slip system a
$\varrho_{GNDe}^a, \varrho_{GNDs}^a$	edge and screw types of GND density in slip system a
$\varrho_{loop}^l, \dot{\varrho}_{loop}^l$	Loop defect density and its evolution rate in defect system l
h^b	self hardening rate (Voce)
h_b^a	latent hardening excluding slip rates
H_b^a	latent hardening matrix (Voce)
h_0	reference hardening rate (Voce)
m	strain hardening exponent (Voce)
s_s	saturated value of CRSS (Voce)
k	linear SSD evolution coefficient
k_1	SSD density multiplication rate (KME)
k_2	SSD annihilation rate (KME)
X^a, \dot{X}^a	back stress and its evolution rate on slip system a
h	kinematic hardening rate (A-F type)
h_D	kinematic softening rate (A-F type)
ζ	scaling factor for back stress (GND-based)
τ_s, τ_s^0	irradiation solute strength and its initial value
Γ_s	cumulative slip at the saturation of irradiation solute strength
ψ	fraction of dislocations that become mobile for irradiated materials
r_l^a	reaction vector between slip in system a and loop defect l
c_l^a	projected reaction between slip and defect

approaches. Spectral methods are fast compared to CPFEM solvers, but they require periodic boundary conditions that limit practical applications, although these effects have been recently addressed by iterative

solutions to satisfy mixed boundary conditions (Kabel et al., 2016). Peridynamics has a limited resolution due to the computationally expensive nonlocal computational scheme and stability issues linked to

d^l	size of loop defect l
N^l	number density of loop defect l
I_l^a	Strain-softening interaction matrix between defect l and slip system a
i_1, i_2	strain-softening interaction coefficients between loop defects and slip systems
J_l^a	Strength interaction matrix between loop defect l and slip system a
j_1, j_2	strength interaction coefficients between loop defect l and slip system a
a, b, c	lattice spacing along three directions for BCT crystal structure
c/a	c-axis ratio for HCP materials
l^a	dislocation line direction on slip system a in the intermediate/undeformed configuration
n_c^a	slip plane normal of slip system a in the undeformed crystal reference
n_e^a	slip plane normal of slip system a in the deformed configuration
n^a	slip plane normal of slip system a in the intermediate/undeformed configuration
t_c^a	line direction of an edge dislocation in slip system a in the undeformed crystal reference
s_c^a	slip direction of slip system a in the undeformed crystal reference
s_e^a	slip direction of slip system a in the deformed configuration
S^a	Schmid tensor of slip system a in the deformed configuration
s^a	slip direction of slip system a in the intermediate/undeformed configuration
C, C_c	4th order elasticity tensor in the deformed and crystal configurations
\mathbb{P}	4th order derivative of plastic strain increment with respect to Cauchy stress
\mathbb{I}	4th order identity tensor

the non-ordinary state-based formulation that is required to adopt the same constitutive models using correspondence models (Silling et al., 2007). Therefore, the use of finite elements is still one of the most widely adopted techniques for modeling polycrystals, especially for industrial applications.

The representativeness of a polycrystal finite element model has received significant attention over the years. It is common to have as many grains in the polycrystalline representative volume element (RVE) (Barbe et al., 2001a,b). Recent studies have employed CPFEM to examine the dimensions and resolution of the RVE, uncovering the dependence of representativeness on varying strain levels (Lim et al., 2019; Chen et al., 2022). Consequently, the RVE must include a sufficient quantity of grains, with each grain being represented by an adequate number of elements to yield results within the anticipated variability.

Different time integration methods for crystal plasticity have been developed over the years. The pioneering work of Huang used slip increments as the primary variable with the residual size as the number of slip systems (Huang, 1991). In that study, the forward-gradient was used as a single-step noniterative linear solution as the predictor and backup solution in addition to a fully-implicit iterative nonlinear

solver. Kalidindi et al. used a semi-implicit time integration scheme based on the 2nd Piola–Kirchoff stress defined in the intermediate configuration (Kalidindi et al., 1992). The major advantage of using the intermediate configuration lies in the fact that it does not require transformation of crystallographic vectors or properties such as the elasticity matrix because the initial lattice orientation does not change after plastic slip (see Fig. 1). In addition, a time-stepping algorithm was proposed to introduce time cutbacks in case of convergence problems. The follow-up studies developed analytical expressions for the tangent stiffness instead of numerical perturbation (Balasubramanian, 1998; Jin et al., 2019). Similarly, Dunne et al. used symmetric Cauchy stress as the primary variable in the deformed configuration, and residual which is also efficient (Dunne et al., 2007). The properties need to be updated for the deformed configuration, but the simplicity of the solver offered a much faster solution. There are also crystal plasticity solvers based on deformation gradients (Maniatty et al., 1992; Sarma and Zacharia, 1999) in which the asymmetry of the residuals leads to larger residual and tangent stiffness expressions, resulting in longer computational times. Plastic strain-based solvers allowed a better response especially when using physics-based models that have a highly nonlinear (exponential or hyperbolic sine) dependence of slip on the stress and consequently more stable convergence behavior than the stress-based CP solvers (Demir and Gutierrez-Urrutia, 2021). An alternative solver based on the inverted slip law was developed to specifically deal with the nearly rate-insensitive slip parameters (Hardie et al., 2023). The plastic velocity gradient has also been adopted as the primary variable in some solvers (Roters et al., 2012). Dawson and Marin implicitly decomposed elastic strain, rotation, and hardness by solving for volumetric and deviatoric stresses separately (Marin and Dawson, 1998), which has been made publicly available (Dawson and Boyce, 2015). Some of these CP solvers (ie DAMASK (Roters et al., 2019), FEPX (Dawson and Boyce, 2015), and MOOSE (Lindsay et al., 2022)) have been widely adopted in many references.

However, despite the ever growing popularity of crystal plasticity modeling, very few studies compare different integration schemes. Liu et al. developed a modified forward gradient approach (Huang, 1991), which revealed a nearly two orders of magnitude reduction in computational time compared to semi-implicit state update methods which rely on the plastic part of the deformation gradient (Maniatty et al., 1992), the elastic part of the deformation gradient (Sarma and Zacharia, 1999) and resolved shear stress (Cuitino and Ortiz, 1993). However, these findings were not compared in a finite element framework. The efficiency of crystal plasticity solvers has been a major concern for many studies (Nehüser and Mosler, 2023). A stable radial return algorithm was found to be the key to robustness (Mánik et al., 2022). Miehe et al. investigated singular value decomposition and numerical perturbation to invert a singular tangent stiffness during a Newton–Raphson iteration to improve the robustness of the CP calculations (Miehe et al., 1999). For 3D polycrystal grain geometries, the grain boundary character and grain neighbor relations were found to be important properties for large deformations (Knezevic et al., 2014) that put computational efficiency and robustness as a top priority.

Data-driven modeling by using machine learning methods in conjunction with crystal plasticity has been a current research focus (Weber et al., 2022; Veasna et al., 2023). Here, polycrystal simulations were coupled with large-scale applications to investigate mechanical behavior and uncertainty quantification (Tallman et al., 2020). Therefore, today's trends in digitization motivate the need for more efficient and robust crystal plasticity solvers.

Studies investigating the effect of the finite element displacement field solver type (i.e. explicit or implicit) and the rate sensitivity of constitutive models also highlighted the presence of other underlying factors on the solution efficiency and robustness. For example, a comparison of a rate-sensitive model to a rate-insensitive model revealed the importance of latent hardening and an interaction matrix in convergence (Prüger and Kiefer, 2020). Implicit finite element solvers

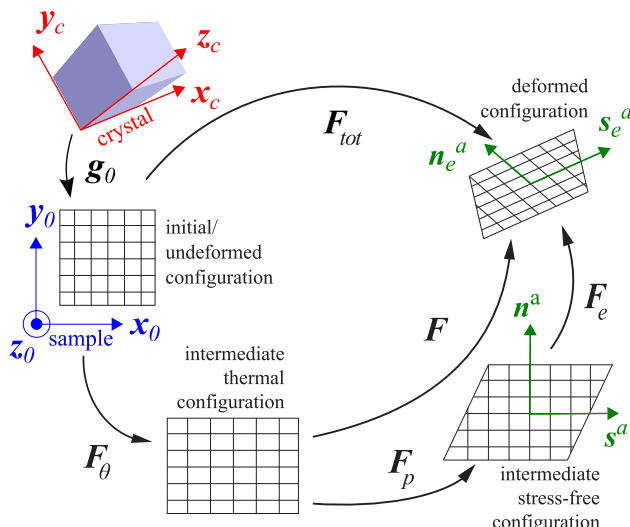


Fig. 1. Multiplicative decomposition of total deformation.

can utilize larger time increments than explicit solver schemes, which offer a faster and a more robust solution, while explicit solvers may have fewer convergence issues for highly non-linear simulations such as contact load cases (Harewood and McHugh, 2007). There is still a lack of understanding of the relative efficiencies of these models, and few systematic comparison studies exist, which use the same finite element field solver and with the same hardening rule.

In this study, a hybrid crystal plasticity integration method was developed and implemented using different state update schemes, namely: linear (non-iterative), explicit, semi-implicit, and fully implicit. Crystal plasticity equations are revisited in detail, including derivations to provide a complete reference for the reader. These formulations have been used in many references, but a complete derivation has not been presented in most of the references; hence provided here alongside the CP code. The framework implemented within a finite element solver is referred to as OXFORD-UMAT. Various alternative materials and models are available for slip, creep, strain hardening, irradiation hardening, length scale dependence, and back stress. The model is validated using single-crystal and large-scale polycrystal simulations. Simulation findings and computational times are compared with those of other crystal plasticity solvers that use the same finite element solver and computational environment (software and hardware), revealing the relative efficiency that can be achieved using the proposed framework.

2. Modeling

In this section, the crystal plasticity kinematics is explained in detail. The formulations are not new, but they are shown with derivations (some of which are missing from the literature) and will help the reader to understand how the equations are solved. The following section explains alternative constitutive models available within the code. The semi-implicit time integration and forward-gradient methods are explained in the following sections.

2.1. Crystal plasticity kinematics

The total deformation gradient, F_{tot} , consists of a mechanical part, F and a thermal part, F_θ as in Eq. (2.1). We used a similar decomposition in the Musinski and McDowell (2015), Hu et al. (2016), Pokharel et al. (2019). This is shown schematically in Fig. 1.

$$F_{tot} = F_e F_p F_\theta. \quad (2.1)$$

The thermal part of the strain increment in the crystal lattice is computed using Eq. (2.2) in which α is the matrix containing the thermal expansion coefficients, $\Delta\theta$ represents the temperature change in the current increment, θ , with respect to the temperature at the former time increment, $\theta(t)$ ¹:

$$\Delta E_\theta^c = \alpha \Delta\theta, \quad \text{in which } \Delta\theta = \theta - \theta(t). \quad (2.2)$$

The thermal expansion coefficient is generalized as in Eq. (2.3) in which $\alpha_1, \alpha_2, \alpha_3$ are the thermal expansion coefficients in the principal Cartesian directions in the lattice frame:

$$\alpha = \begin{bmatrix} \alpha_1 & 0 & 0 \\ 0 & \alpha_2 & 0 \\ 0 & 0 & \alpha_3 \end{bmatrix}, \quad (2.3)$$

The thermal eigenstrain can be anisotropic, especially for non-cubic materials, which is accounted for in the framework. The increment in thermal strain is transformed to the sample reference using the crystal-to-sample (initial/undeformed) transformation, g_0 , using Eq. (2.4) in direct notation:

$$\Delta E_\theta = g_0 \Delta E_\theta^c g_0^T, \quad (2.4)$$

The thermal deformation gradient is initially set to the identity matrix I and computed incrementally using:

$$F_\theta = F_\theta(t) + \Delta E_\theta. \quad (2.5)$$

The mechanical part of the deformation gradient reads:

$$F = F_{tot} F_\theta^{-1}. \quad (2.6)$$

The total velocity gradient, L , is computed from the mechanical part of the deformation gradient using:

$$L = F F^{-1}. \quad (2.7)$$

The rate of change of deformation gradient is approximately calculated using:

$$\dot{F} = \frac{F - F(t)}{\Delta t}. \quad (2.8)$$

The symmetric part gives the total strain rate (rate of deformation) namely:

$$D = \frac{L + L^T}{2}. \quad (2.9)$$

This is then used to compute the total strain increment:

$$\Delta e = D \Delta t. \quad (2.10)$$

The total spin is computed from the anti-symmetric part of the velocity gradient:

$$\Omega = \frac{L - L^T}{2}. \quad (2.11)$$

The mechanical deformation gradient, F , consists of elastic, F_e , and plastic parts, F_p :

$$F = F_e F_p. \quad (2.12)$$

With volume remaining constant during plastic deformation, Eq. (2.13):

$$\det(F_p) = 1. \quad (2.13)$$

The plastic velocity gradient is obtained by transforming the slip rates, $\dot{\gamma}^a$, followed by summing the individual contributions from each slip system (The derivation is shown Appendix C):

$$L_p = \sum_a \dot{\gamma}^a s^a \otimes n^a. \quad (2.14)$$

¹ Brackets (*t*) indicate the quantities that belong to the former time increment while the rest of quantities without a bracket belong to the current time increment *t* + Δ*t* which is omitted for brevity.

The Schmid tensor in the deformed configuration, S^a , for the slip system a is defined as in Eq. (2.15). The Schmid tensor in the slip reference frame is prescribed by the deformed slip direction,² s_e^a , and deformed slip plane normal, n_e^a :

$$S^a = s_e^a \otimes n_e^a. \quad (2.15)$$

Eq. (2.16) transforms the slip direction to the deformed reference:

$$s_e^a = F_e s^a. \quad (2.16)$$

Eq. (2.17) transforms the slip plane normal ensuring it remains orthogonal to the slip direction during deformation:

$$n_e^a = F_e^{-T} n^a. \quad (2.17)$$

The total velocity gradient can be expressed as the sum of the symmetric strain rate, D , and anti-symmetric total spin tensors, Ω :

$$L = D + \Omega. \quad (2.18)$$

The total stretch rate can be decomposed into its elastic and plastic parts:

$$D = D_e + D_p. \quad (2.19)$$

Similarly, the total spin (continuum spin)³ can be decomposed into its elastic and plastic parts:

$$\Omega = \Omega_e + \Omega_p. \quad (2.20)$$

The elastic part of the velocity gradient in the deformed configuration becomes:

$$L_e = \Omega_e + D_e. \quad (2.21)$$

Using Eq. (2.14), the plastic velocity gradient can be expressed as:

$$\Omega_p + D_p = \sum_a \dot{\gamma}^a s^a \otimes n^a. \quad (2.22)$$

2.2. Constitutive laws

Hill and Rice obtained the Jaumann rate of stress using (Hill and Rice, 1972a):

$$\nabla \sigma_e + \sigma \operatorname{tr}(D_e) = \mathbb{C} : D_e. \quad (2.23)$$

Elasticity relates the rotation-free objective Jaumann rate of stress, σ_e , to the elastic deformation rate approximately:

$$\nabla \sigma_e \approx \mathbb{C} : D_e. \quad (2.24)$$

The stress rate, $\dot{\sigma}$, in terms of the Jaumann rate of stress is given by:

$$\dot{\sigma} = \nabla \sigma_e + \Omega_e \sigma(t) - \sigma(t) \Omega_e. \quad (2.25)$$

A more accurate relation is provided by Hill and Rice with an additional term accounting for the volumetric changes (Hill and Rice, 1972b):

$$\dot{\sigma} = \nabla \sigma_e + \operatorname{tr}(D_e) \sigma(t) + \Omega_e \sigma(t) - \sigma(t) \Omega_e. \quad (2.26)$$

$[\mathbb{C}]$ is the elastic stiffness matrix in direct notation^{4, 5} corresponding to the 4th order elasticity tensor, \mathbb{C} , in the deformed configuration. $[\mathbb{C}]$

² The subscript e used for the slip vectors denote the final deformed configuration after the elastic deformation.

³ Continuum spin, Ω , can be written in terms of the rotation rate, \dot{R} , and rotation, R , as $\Omega = \dot{R} R^T$.

⁴ Curly brackets, {}, and square brackets, [], stand for the representation in direct/vectorized/Voigt notation of 2nd rank and 4th rank tensors in terms of vectors and matrices, respectively.

⁵ The vectorization of a second rank tensor has the order: $\{a\} = \{a_{11} \ a_{22} \ a_{33} \ a_{12} \ a_{13} \ a_{23}\}^T$.

is obtained by transformation of elasticity in the crystal reference, $[\mathbb{C}^c]$, to the sample or deformed reference in direct notation using:

$$[\mathbb{C}] = [\mathbf{G}] [\mathbb{C}^c] [\mathbf{G}]^T. \quad (2.27)$$

$[\mathbf{G}]$ is the 6×6 special 4th rank transformation in matrix form⁶ to transform vectorized stresses from the crystal reference to the sample reference using the components of the crystal to sample transformation, \mathbf{g} , according to Bond (1943) is given in Box I.

The elastic stiffness matrix in the crystal reference is given by Eq. (2.29) for a cubic material with three independent elastic constants C_{11} , C_{12} , and C_{44} in direct notation as:

$$[\mathbb{C}^c] = \begin{bmatrix} C_{11} & C_{12} & C_{12} & 0 & 0 & 0 \\ C_{12} & C_{11} & C_{12} & 0 & 0 & 0 \\ C_{12} & C_{12} & C_{11} & 0 & 0 & 0 \\ 0 & 0 & 0 & C_{44} & 0 & 0 \\ 0 & 0 & 0 & 0 & C_{44} & 0 \\ 0 & 0 & 0 & 0 & 0 & C_{44} \end{bmatrix}. \quad (2.29)$$

The constitutive laws for slip, creep, strain hardening, back stress, and strain gradients will be explained in the results section showing the effect of parameters and comparison of different forms.

2.3. Crystal plasticity solver based on Cauchy stress

The main crystal plasticity solver is based on the solution method developed by Dunne et al. (2007). The formulation is based on the deformed vectors, and the main quantity to be solved is the Cauchy stress. Eq. (2.24) governs the stress in the deformed configuration. The elastic strain is obtained by summing the former elastic strain with the elastic strain increment.

$$\epsilon_e = \epsilon_e(t) + \Delta \epsilon_e. \quad (2.30)$$

Total strain increment is the sum of elastic and plastic strain increments which gives:

$$\Delta \epsilon_e = \Delta \epsilon - \Delta \epsilon_p. \quad (2.31)$$

Substituting Eqs. (2.30) and (2.31) into Hooke's law, using the anisotropic elasticity tensor, \mathbb{C} , at the deformed configuration, gives the trial stress and the plastic corrector:

$$\sigma = \mathbb{C} : (\epsilon_e(t) + \Delta \epsilon) - \mathbb{C} : \Delta \epsilon_p. \quad (2.32)$$

The residual Cauchy stress, ψ , is minimized by the Newton–Raphson method:

$$\psi = \sigma - \sigma_{tr} + \mathbb{C} : \Delta \epsilon_p = 0. \quad (2.33)$$

where the trial stress:

$$\sigma_{tr} = \mathbb{C} : (\epsilon_e(t) + \Delta \epsilon). \quad (2.34)$$

The total plastic strain increment is obtained by summing up the slip rates with the Schmid tensor in the deformed configuration which

⁶ The strain in the sample reference, ϵ , is transformed to the crystal reference, ϵ^c , by using the inverse of the crystal to sample transformation, \mathbf{g} , as: $\epsilon_{ij}^c = (g^T)_{im} (g^T)_{jn} \epsilon_{mn}$. Note the transpose of rotations implies the inverse due to orthogonality. The elasticity applied at the crystal reference gives the stress at the crystal reference: $\sigma_{ij}^c = \mathbb{C}_{ijmn}^c \epsilon_{mn}^c$. Transforming the stress in the crystal reference back to the sample reference: $\sigma_{ij} = g_{im} g_{jn} \sigma_{mn}^c$. Overall relation between stress and strain at the sample reference becomes: $\sigma_{ij} = g_{im} g_{jn} \mathbb{C}_{mnop}^c (g^T)_{ok} (g^T)_{pl} \epsilon_{kl}$, which reduces to: $\sigma_{ij} = (g_{im} g_{jn} g_{ko} g_{lp} \mathbb{C}_{mnop}^c) \epsilon_{kl}$. The elasticity in sample reference in direct notation becomes: $[\mathbb{C}] = [\mathbf{g} \otimes \mathbf{g}] [\mathbb{C}^c] [\mathbf{g}^T \otimes \mathbf{g}^T]$ which equivalently defines the elasticity matrix transformation in direct notation: $[\mathbb{C}] = [\mathbf{G}] [\mathbb{C}^c] [\mathbf{G}]^T$. Therefore the dyadic, \mathbf{G} , transforms the stress from the crystal to the sample: $\mathbf{G} = \mathbf{g} \otimes \mathbf{g}$.

$$[\mathbf{G}] = \begin{bmatrix} g_{11}^2 & g_{12}^2 & g_{13}^2 & 2g_{11}g_{12} & 2g_{13}g_{11} & 2g_{12}g_{13} \\ g_{21}^2 & g_{22}^2 & g_{23}^2 & 2g_{21}g_{22} & 2g_{23}g_{21} & 2g_{22}g_{23} \\ g_{31}^2 & g_{32}^2 & g_{33}^2 & 2g_{31}g_{32} & 2g_{33}g_{31} & 2g_{32}g_{33} \\ g_{11}g_{21} & g_{12}g_{22} & g_{13}g_{23} & g_{11}g_{22} + g_{12}g_{21} & g_{13}g_{21} + g_{11}g_{23} & g_{12}g_{23} + g_{13}g_{22} \\ g_{31}g_{11} & g_{32}g_{12} & g_{33}g_{13} & g_{11}g_{32} + g_{12}g_{31} & g_{13}g_{31} + g_{11}g_{33} & g_{12}g_{33} + g_{13}g_{32} \\ g_{21}g_{31} & g_{22}g_{32} & g_{23}g_{33} & g_{22}g_{31} + g_{21}g_{32} & g_{21}g_{33} + g_{23}g_{31} & g_{22}g_{33} + g_{23}g_{32} \end{bmatrix}. \quad (2.28)$$

Box I.

leads to the anisotropy of the plastic flow direction, [Appendix C](#). The plastic strain increment, $\Delta\epsilon_p$, is the sum of the slip increments in the deformed reference considering the stretch (symmetric) part of the plastic velocity gradient:

$$\Delta\epsilon_p = \text{sym} \left(\sum_a \dot{\gamma}^a S^a \right) \Delta t. \quad (2.35)$$

Differentiation of the residual [\(2.33\)](#) with respect to the Cauchy stress gives:

$$\frac{\partial \psi}{\partial \sigma} = \mathbb{I} + \mathbb{C} : \mathbb{P}. \quad (2.36)$$

\mathbb{P} is obtained by differentiating plastic strain increment [\(2.35\)](#) with respect to the Cauchy stress and using the chain-rule:

$$\mathbb{P} = \frac{\partial \text{sym}(\sum_a \dot{\gamma}^a S^a)}{\partial \sigma} \Delta t = \text{sym} \left(\sum_a \frac{\partial \dot{\gamma}^a}{\partial \tau^a} S^a \frac{\partial \tau^a}{\partial \sigma} \right) \Delta t. \quad (2.37)$$

Note the derivative of resolved shear stress with respect to the stress simply gives the Schmid tensor:

$$\frac{\partial \tau^a}{\partial \sigma} = S^a, \quad \text{since } \tau^a = S^a : \sigma. \quad (2.38)$$

Substituting Eq. [\(2.38\)](#) into Eq. [\(2.37\)](#) gives the expression for the \mathbb{P} matrix:

$$\mathbb{P} = \text{sym} \left(\sum_a \frac{\partial \dot{\gamma}^a}{\partial \tau^a} S^a \otimes S^a \right) \Delta t. \quad (2.39)$$

Newton–Raphson solution requires the value and the derivative of the residual function. The residual in vectorized form and its derivative with respect to stress give the stress increment:

$$\{\Delta\sigma\} = - \left[\frac{\partial \psi}{\partial \sigma} \right]^{-1} \cdot \{\psi\}. \quad (2.40)$$

Substituting Eqs. [\(2.33\)](#) and [\(2.36\)](#) to Eq. [\(2.40\)](#), gives the expression for the stress increment in direct notation as:

$$\{\Delta\sigma\} = -[\mathbb{I} + \mathbb{C} \cdot \mathbb{P}]^{-1} \cdot \{\sigma - \sigma_{tr} + \mathbb{C} \cdot \Delta\epsilon_p\}. \quad (2.41)$$

The stress is updated at each increment (i) using Newton–Raphson method until the norm of the vectorized stress increment gets smaller than a tolerance, i.e., for the present work $\|\{\Delta\sigma\}\| < 10^{-8}$ MPa:

$$\sigma^{(i+1)} = \sigma^{(i)} + \Delta\sigma^{(i)}. \quad (2.42)$$

Additionally, the stress increment threshold that was introduced in [Kalidindi et al. \(1992\)](#) was used to enhance convergent behavior. This correction applies in case the increment of stress becomes larger than a threshold,⁷ f . The stress increment is then set to a fraction of the average value of the CRSS, $\bar{\tau}_c$, because the CRSS can vary significantly

between slip systems (e.g., in an HCP material). Therefore, the stress correction at the i th iteration is:

$$\Delta\sigma^{(i)} = \begin{cases} f \bar{\tau}_c \text{sgn}(\Delta\sigma^{(i)}), & \text{if } \|\Delta\sigma^{(i)}\| > f \bar{\tau}_c, \\ \Delta\sigma, & \text{otherwise.} \end{cases} \quad (2.43)$$

The initial stress guess, σ^0 , for the stress solver is of particular importance because the Newton–Raphson method converges if and only if the initial guess is within the interval of convergence. The initial guess is obtained by the forward-gradient approach, or from the weighted average of the fully elastic (σ_{tr}) and fully plastic ($\sigma(t)$) guesses as in Eq. [\(2.44\)](#). As shown in [Hardie et al. \(2023\)](#), we confirm that the fully plastic guess ($\phi = 1$) reveals a much better convergence response than the trial stress (fully elastic guess, $\phi = 0$) or any other combined initial guess:

$$\sigma^0 = (1 - \phi)\sigma_{tr} + \phi\sigma(t). \quad (2.44)$$

Once the slip rates are computed, the corresponding states (hardening or softening) can be updated either by explicit, semi-implicit, or fully-implicit state update methods.

2.3.1. Semi-implicit state update

In addition to the stress iteration, a second outer-level loop is utilized (see [Fig. 2](#)) to account for changes in the states and the corresponding changes in the slip rates. For generality, the symbol Y^a represents any state variable(s), including the critical resolved shear stress, τ_c^a , solute strength, τ_s , statistically-stored dislocation density, ρ_{SSD} , and density of loop defects, ρ_{loop} . The increment in the state variable is calculated using the corresponding evolution laws (ex. strain hardening models) from the rate of evolution, \dot{Y}^a , as:

$$\Delta Y^a = \dot{Y}^a \Delta t. \quad (2.45)$$

The states are updated according to Euler time integration with Eq. [\(2.46\)](#) which makes the overall scheme a semi-implicit method ([Kalidindi et al., 1992](#)):

$$(Y^a)^{l+1} = (Y^a)^l + (\Delta Y^a)^l. \quad (2.46)$$

The state variables contribute to the effective CRSS, τ_{eff}^a therefore, the outer loop iteration is assumed to converge when the increment in CRSS becomes less than a tolerance (e.g., $|\Delta\tau_{eff}^a| < 10^{-5} \times \tau_{eff}^0$ in the present study).

2.3.2. Material tangent

The finite element solver requires a material tangent to perform the Newton–Raphson iteration to solve equilibrium. The material tangent does not affect the solution, but it affects the convergence rate of the displacement field solution. The material tangent is the derivative of the stress increment with respect to the total strain increment, $\frac{\partial \Delta\sigma}{\partial \Delta\epsilon}$. Taking the variation of the residual in Eq. [\(2.33\)](#) with respect to stress gives:

$$\partial\sigma - \partial\sigma_{tr} + \mathbb{C} : \partial\Delta\epsilon_p = \mathbf{0}. \quad (2.47)$$

⁷ The recommended value for threshold factor, f , was $\frac{2}{3}$ in [Kalidindi et al. \(1992\)](#).

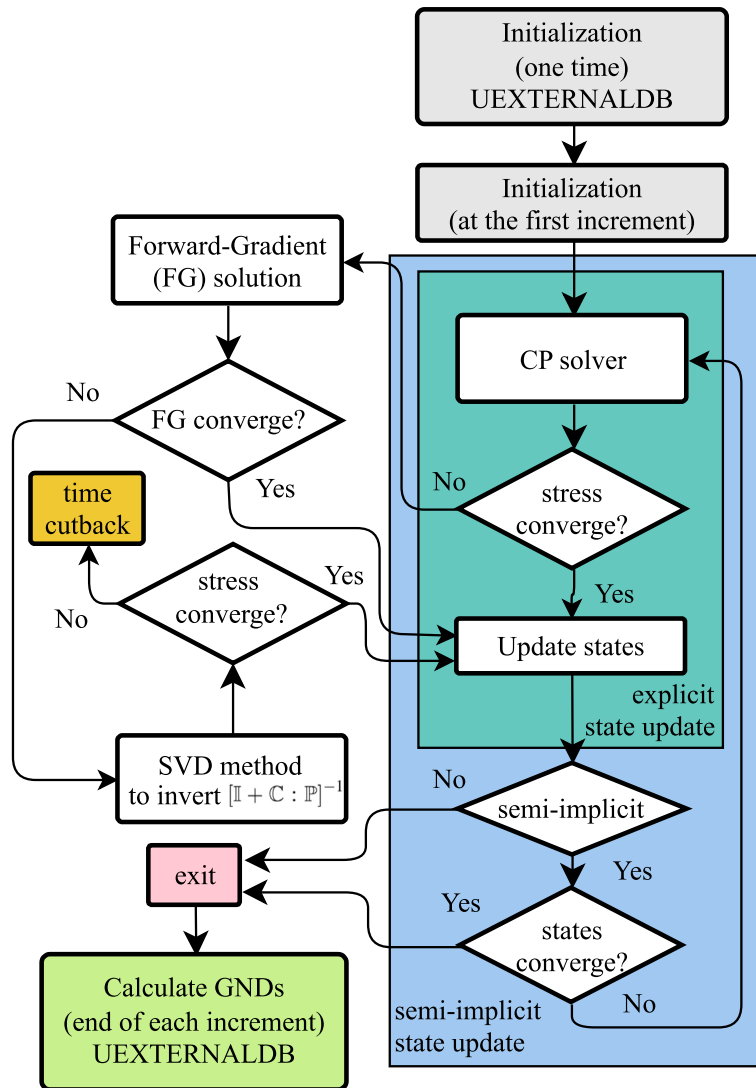


Fig. 2. Algorithm flow chart for the crystal plasticity solver.

The variation of stress becomes $\partial\sigma = \partial\sigma(t) + \partial\Delta\sigma = \partial\Delta\sigma$ as the old stress at t is constant. The variation of trial stress becomes:

$$\partial\sigma_{tr} = C : \partial[\epsilon_e(t) + \Delta\epsilon] = C : \partial\Delta\epsilon. \quad (2.48)$$

The variation of the plastic strain increment becomes:

$$\partial\Delta\epsilon_p = P : \partial\sigma = P : \partial\Delta\sigma. \quad (2.49)$$

Substituting Eqs. (2.48) and (2.49) to Eq. (2.47) gives the second rank equation:

$$\partial\Delta\sigma - C : \partial\Delta\epsilon + C : P : \partial\Delta\sigma = 0. \quad (2.50)$$

Re-arranging terms reveal Eq. (2.51) for the material tangent in direct notation (or tangent stiffness matrix) in which I is the 4th order identity tensor:

$$\left[\frac{\partial\Delta\sigma}{\partial\Delta\epsilon} \right] = [I + C \cdot P]^{-1} \cdot [C]. \quad (2.51)$$

The tangent stiffness in (2.51) is required as a user output in UMAT which is defined by the variable 'DDSDDE'. This is required to solve for the displacement field in the presence of geometrical and/or material nonlinearity.

2.4. Forward-gradient method (linear)

Forward-gradient method (linear) is a noniterative single-step crystal plasticity solution that uses slip increments as variables. This scheme helps in two important ways:

- Provides an accurate initial guess for the iterative method
- Gives a backup solution in case the stress-based iterative method diverges.

The scheme uses the Jaumann stress rate that represents the stress state rotating with the crystal reference in Eq. (2.52):

$$\nabla \sigma_e = \dot{\sigma} - \Omega_e \sigma + \sigma \Omega_e. \quad (2.52)$$

Co-rotational stress on axes that rotate with the material is given by Eq. (2.53):

$$\nabla \sigma = \dot{\sigma} - \Omega \sigma + \sigma \Omega. \quad (2.53)$$

Subtraction of Eq. (2.53) from Eq. (2.52) gives:

$$\nabla \sigma_e = \nabla \sigma + (\Omega - \Omega_e) \sigma - \sigma (\Omega - \Omega_e). \quad (2.54)$$

which, using the identity in Eq. (2.20), is:

$$\nabla \sigma_e = \nabla \sigma + \Omega_p \sigma - \sigma \Omega_p. \quad (2.55)$$

Eq. (2.19) also gives Eq. (2.56):

$$\mathbf{D}_e = \mathbf{D} - \mathbf{D}_p. \quad (2.56)$$

Using the identity in Eq. (2.56), the trace can be computed using only the elastic strain rate as in Eq. (2.57) assuming isochoric plastic deformation:

$$\text{tr}(\mathbf{D}) = \text{tr}(\mathbf{D}_e). \quad (2.57)$$

Substituting the (2.56), (2.55) and (2.57) into the Eq. (2.23) in order to replace the expressions for \mathbf{D}_e and $\overset{\nabla}{\sigma}_e$ with \mathbf{D} and $\overset{\nabla}{\sigma}$, respectively gives:

$$\overset{\nabla}{\sigma} + \Omega_p \sigma - \sigma \Omega_p + \sigma \text{tr}(\mathbf{D}) = \mathbb{C} : (\mathbf{D} - \mathbf{D}_p). \quad (2.58)$$

Re-arranging terms, Eq. (2.58) can be written as:

$$\overset{\nabla}{\sigma} = \mathbb{C} : \mathbf{D} - \sigma \text{tr}(\mathbf{D}) - \mathbb{C} : \mathbf{D}_p - \Omega_p \cdot \sigma + \sigma \cdot \Omega_p. \quad (2.59)$$

2.4.1. Incremental formulation

Multiplying both sides of Eq. (2.59) with the time increment gives the stress increment:

$$\Delta\sigma = \mathbb{C} : \Delta\epsilon - \sigma \text{tr}(\Delta\epsilon) - (\mathbb{C} : \mathbf{D}_p + \Omega_p \cdot \sigma - \sigma \cdot \Omega_p) \Delta t. \quad (2.60)$$

The symmetric, \mathbf{P}^a , and anti-symmetric, \mathbf{W}^a , parts of the Schmid tensor define the stretch rate and spin tensors. Note that \mathbf{P}^a is not to be confused with the 4th order tensor \mathbb{P}^a :

$$\mathbf{P}^a = \frac{1}{2} (\mathbf{s}_e^a \otimes \mathbf{n}_e^a + \mathbf{n}_e^a \otimes \mathbf{s}_e^a). \quad (2.61)$$

$$\mathbf{W}^a = \frac{1}{2} (\mathbf{s}_e^a \otimes \mathbf{n}_e^a - \mathbf{n}_e^a \otimes \mathbf{s}_e^a). \quad (2.62)$$

Therefore, the corresponding plastic stretch rate (2.63) and plastic spin tensors (2.64) are computed using the slip rates as follows:

$$\mathbf{D}_p = \sum_a \mathbf{P}^a \dot{\gamma}^a. \quad (2.63)$$

$$\Omega_p = \sum_a \mathbf{W}^a \dot{\gamma}^a. \quad (2.64)$$

These rate forms are multiplied by the time increment to represent their change in terms of the plastic slip increment $\Delta\gamma^a$:

$$\mathbf{D}_p \Delta t = \sum_a \mathbf{P}^a \Delta\gamma^a. \quad (2.65)$$

$$\Omega_p \Delta t = \sum_a \mathbf{W}^a \Delta\gamma^a. \quad (2.66)$$

Substituting Eqs. (2.65) and (2.66) into the stress increment in Eq. (2.60) gives:

$$\Delta\sigma = \mathbb{C} : \Delta\epsilon - \sigma \text{tr}(\Delta\epsilon) - \sum_a (\mathbb{C} : \mathbf{P}^a + \mathbf{W}^a \cdot \sigma - \sigma \cdot \mathbf{W}^a) \Delta\gamma^a. \quad (2.67)$$

A relation for the increment in resolved shear stress (RSS) is given by the projection of Cauchy stress on to slip system a :

$$\tau^a = \mathbf{S}^a : \sigma = \mathbf{s}_e^a \cdot \sigma \cdot \mathbf{n}_e^a. \quad (2.68)$$

By taking the time derivative of Eq. (2.68), using the chain rule of differentiation and using the symmetric property of Cauchy stress ($\sigma = \sigma^T$), Eq. (2.69) can be obtained (Appendix D shows the derivation for the rate of change of slip direction and slip plane normal):

$$\dot{\tau}^a = \mathbf{s}_e^a \cdot (\dot{\sigma} - \mathbf{L}_e \cdot \sigma + \sigma \cdot \mathbf{L}_e) \cdot \mathbf{n}_e^a. \quad (2.69)$$

The velocity gradient can be decomposed into stretch rate and spin as:

$$\mathbf{L}_e = \mathbf{D}_e + \Omega_e. \quad (2.70)$$

Substituting Eq. (2.70) into (2.69) gives:

$$\dot{\tau}^a = \mathbf{s}_e^a \cdot [(\dot{\sigma} - \Omega_e \cdot \sigma + \sigma \cdot \Omega_e) - \mathbf{D}_e \cdot \sigma + \sigma \cdot \mathbf{D}_e] \cdot \mathbf{n}_e^a. \quad (2.71)$$

Using the expression for the Jaumann rate of stress (2.52) together with Eq. (2.71) gives:

$$\dot{\tau}^a = \mathbf{s}_e^a \cdot (\overset{\nabla}{\sigma}_e - \mathbf{D}_e \cdot \sigma + \sigma \cdot \mathbf{D}_e) \cdot \mathbf{n}_e^a. \quad (2.72)$$

The symmetric Cauchy stress and the symmetric elastic stretch rate together with the properties of the inner product⁸ gives:

$$\begin{aligned} -\mathbf{S}_e^a : \mathbf{D}_e \cdot \sigma &= -\mathbf{S}_e^a \cdot \sigma^T : \mathbf{D}_e = -(\mathbf{S}_e^a \cdot \sigma^T)^T : \mathbf{D}_e^T = \\ &- \sigma \cdot (\mathbf{S}^a)^T : \mathbf{D}_e = -(\mathbf{S}^a)^T : \sigma^T \cdot \mathbf{D}_e = -(\mathbf{S}^a)^T : \sigma \cdot \mathbf{D}_e. \end{aligned} \quad (2.73)$$

Further simplification of Eq. (2.72), using the property in (2.73) and re-arranging terms gives:

$$\dot{\tau}^a = \mathbf{S}^a : \overset{\nabla}{\sigma}_e + [\mathbf{S}^a - (\mathbf{S}^a)^T] : \sigma \cdot \mathbf{D}_e. \quad (2.74)$$

Eq. (2.62) can be used to replace the Schmid tensor with the plastic spin as:

$$\mathbf{S}^a - (\mathbf{S}^a)^T = 2\mathbf{W}^a. \quad (2.75)$$

Substituting (2.24) and (2.75) into Eq. (2.74) gives:

$$\dot{\tau}^a = (\mathbf{S}^a : \mathbb{C} + 2\mathbf{W}^a \cdot \sigma) : \mathbf{D}_e. \quad (2.76)$$

The symmetry of σ , \mathbf{D}_e and antisymmetry of \mathbf{W}^a together with the properties of the inner product gives the following equalities:

$$\mathbf{W}^a \cdot \sigma : \mathbf{D}_e = (\mathbf{W}^a \cdot \sigma)^T : \mathbf{D}_e^T = \sigma^T \cdot (\mathbf{W}^a)^T : \mathbf{D}_e = -\sigma \cdot \mathbf{W}^a : \mathbf{D}_e. \quad (2.77)$$

Using the property in (2.77) with (2.76):

$$\dot{\tau}^a = (\mathbf{S}^a : \mathbb{C} + \mathbf{W}^a \cdot \sigma - \sigma \cdot \mathbf{W}^a) : \mathbf{D}_e. \quad (2.78)$$

Note that from Eq. (2.15), (2.61), and (2.62), the Schmid tensor can be expressed in terms of the symmetric plastic stretch rate and anti-symmetric plastic spin coefficient tensors:

$$\mathbf{S}^a = \mathbf{P}^a + \mathbf{W}^a. \quad (2.79)$$

The symmetry of the elasticity tensor (in index notation: $\mathbb{C}_{ijmn} = \mathbb{C}_{ijnm} = \mathbb{C}_{mnni}$) reveals:

$$\mathbf{S}^a : \mathbb{C} = (\mathbf{S}^a)^T : \mathbb{C}. \quad (2.80)$$

Using this in Eq. (2.79) gives:

$$\mathbf{P}^a : \mathbb{C} + \mathbf{W}^a : \mathbb{C} = (\mathbf{P}^a)^T : \mathbb{C} + (\mathbf{W}^a)^T : \mathbb{C} = \mathbf{P}^a : \mathbb{C} - \mathbf{W}^a : \mathbb{C}. \quad (2.81)$$

which is true if and only if:

$$\mathbf{W}^a : \mathbb{C} = -\mathbf{W}^a : \mathbb{C} = 0 \quad (2.82)$$

It follows that the antisymmetric spin part of deformation does not contribute to the strain energy and (2.78) reduces to:

$$\dot{\tau}^a = (\mathbf{P}^a : \mathbb{C} + \mathbf{W}^a \cdot \sigma - \sigma \cdot \mathbf{W}^a) : \mathbf{D}_e. \quad (2.83)$$

Substituting Eq. (2.19) into Eq. (2.83) and using symmetric properties of elasticity tensor gives:

$$\dot{\tau}^a = (\mathbb{C} : \mathbf{P}^a + \mathbf{W}^a \cdot \sigma - \sigma \cdot \mathbf{W}^a) : (\mathbf{D} - \mathbf{D}_p) \quad (2.84)$$

and substituting the expression for the plastic strain rate as the sum of slip rates in Eq. (2.63) gives:

$$\dot{\tau}^a = (\mathbb{C} : \mathbf{P}^a + \mathbf{W}^a \cdot \sigma - \sigma \cdot \mathbf{W}^a) : (\mathbf{D} - \sum_b \mathbf{P}^b \dot{\gamma}^b). \quad (2.85)$$

⁸ $\mathbf{A} : \mathbf{B} = A_{ij} B_{ij} = \mathbf{A}^T : \mathbf{B}^T = A_{ji} B_{ji} = \mathbf{A}\mathbf{B}^T : \mathbf{I} = A_{ij} B_{kj} \delta_{ik}$.

Finally multiplying with the time increment gives the expression for the increment in RSS with respect to the increments of total strain and slip:

$$\Delta\tau^a = (\mathbb{C} : \mathbf{P}^a + \mathbf{W}^a \cdot \boldsymbol{\sigma} - \boldsymbol{\sigma} \cdot \mathbf{W}^a) : (\Delta\epsilon - \sum_b \mathbf{P}^b \Delta\gamma^b). \quad (2.86)$$

This equation is essentially needed to employ the forward-gradient solution that is shown in Section 2.4.2 in Eq. (2.89). Once the RSS increment is represented in terms of the slip increments as in (2.86), the solution for the new slip increments can be obtained.

2.4.2. Time integration

The slip increment, $\Delta\gamma^a$, is simply the difference between the current slip, γ^a , and the slip at the former time step, $\gamma^a(t)$:

$$\Delta\gamma^a = \gamma^a - \gamma^a(t). \quad (2.87)$$

The solution is approximated with linear interpolation using a scalar variable ϑ as in Eq. (2.88). When ϑ is zero, the solution is an explicit Euler solution whereas if ϑ is one, it is an implicit solution:

$$\Delta\gamma^a = \Delta t [(1 - \vartheta)\dot{\gamma}^a(t) + \vartheta\dot{\gamma}^a]. \quad (2.88)$$

Taylor series expansion of slip rates about the current RSS and CRSS ignoring higher order terms gives:

$$\dot{\gamma}^a = \dot{\gamma}^a(t) + \frac{\partial\dot{\gamma}^a}{\partial\tau^a} \Delta\tau^a + \frac{\partial\dot{\gamma}^a}{\partial\tau_c^a} \Delta\tau_c^a. \quad (2.89)$$

Substituting (2.89) as the slip rate term into (2.88) gives:

$$\Delta\gamma^a = \Delta t \left[(1 - \vartheta)\dot{\gamma}^a(t) + \vartheta \left(\dot{\gamma}^a(t) + \frac{\partial\dot{\gamma}^a}{\partial\tau^a} \Delta\tau^a + \frac{\partial\dot{\gamma}^a}{\partial\tau_c^a} \Delta\tau_c^a \right) \right] \quad (2.90)$$

which simplifies to:

$$\Delta\gamma^a = \Delta t \left(\dot{\gamma}^a(t) + \vartheta \frac{\partial\dot{\gamma}^a}{\partial\tau^a} \Delta\tau^a + \vartheta \frac{\partial\dot{\gamma}^a}{\partial\tau_c^a} \Delta\tau_c^a \right). \quad (2.91)$$

Note that we have already obtained an expression for $\Delta\tau^a$ in Eq. (2.86). $\Delta\tau_c^a$ can be calculated from strain hardening equations analytically. For example, assuming a Voce-type hardening expression in Eq. (2.92) in which h_0 , s_s , n , H_b^a represent the hardening rate, saturation value of CRSS, hardening exponent, and latent hardening matrix, respectively, the CRSS rate becomes:

$$\dot{\tau}_c^a = H_b^a \left(1 - \frac{\tau_c^a}{s_s} \right)^n |\dot{\gamma}^b|. \quad (2.92)$$

The increment of CRSS is obtained by multiplying (2.92) by the time increment:

$$\Delta\tau_c^a = H_b^a \left(1 - \frac{\tau_c^a}{s_s} \right)^n \operatorname{sgn}(\dot{\gamma}(t)) \Delta\gamma^b. \quad (2.93)$$

The overall expression for hardening can be simplified by h_b^a as:

$$\Delta\tau_c^a = h_b^a \operatorname{sgn}(\dot{\gamma}(t)) \Delta\gamma^b. \quad (2.94)$$

Substituting the expressions $\Delta\tau^a$ in Eq. (2.86) and $\Delta\tau_c^a$ in Eq. (2.94) into the forward-gradient solution for slip increments $\Delta\gamma^a$ in Eq. (2.91) gives:

$$\begin{aligned} \Delta\gamma^a &= \Delta t \dot{\gamma}^a(t) + \Delta t \vartheta \frac{\partial\dot{\gamma}^a}{\partial\tau^a} (\mathbb{C} : \mathbf{P}^a + \mathbf{W}^a \cdot \boldsymbol{\sigma} - \boldsymbol{\sigma} \cdot \mathbf{W}^a) : (\Delta\epsilon - \sum_a \mathbf{P}^b \Delta\gamma^b) \\ &\quad + \Delta t \vartheta \frac{\partial\dot{\gamma}^a}{\partial\tau_c^a} h_b^a \operatorname{sgn}(\dot{\gamma}(t)) \Delta\gamma^b. \end{aligned} \quad (2.95)$$

Rearranging terms by taking the unknown slip increments $\Delta\gamma^b$ to one side of the equation reveals Eq. (2.96) in which δ_b^a is the identity matrix or Kronecker delta with dimensions equal to the number of slip systems. Note that the square and curly brackets represent matrix and vectors in direct notation, in this case with the size of the number of slip systems:

$$\begin{aligned} &\left[\delta_b^a + \vartheta \Delta t \frac{\partial\dot{\gamma}^a}{\partial\tau^a} (\mathbb{C} : \mathbf{P}^a + \mathbf{W}^a \cdot \boldsymbol{\sigma} - \boldsymbol{\sigma} \cdot \mathbf{W}^a) : \mathbf{P}^b - \vartheta \Delta t \frac{\partial\dot{\gamma}^a}{\partial\tau_c^a} h_b^a \operatorname{sgn}(\dot{\gamma}(t)) \right] \{ \Delta\gamma^b \} \\ &= \left\{ \Delta t \dot{\gamma}^a(t) + \vartheta \Delta t \frac{\partial\dot{\gamma}^a}{\partial\tau^a} (\mathbb{C} : \mathbf{P}^a + \mathbf{W}^a \cdot \boldsymbol{\sigma} - \boldsymbol{\sigma} \cdot \mathbf{W}^a) : \Delta\epsilon \right\}. \end{aligned} \quad (2.96)$$

Therefore, the forward-gradient method is simply the linear solution of Eq. (2.97):

$$[\mathbf{N}_b^a] \{ \Delta\gamma^b \} = \{ \xi^a \}. \quad (2.97)$$

where $[\mathbf{N}_b^a]$ is the known square coefficient matrix with the size being equal to the number of the slip systems:

$$[\mathbf{N}_b^a] = \left[\delta_b^a + \vartheta \Delta t \frac{\partial\dot{\gamma}^a}{\partial\tau^a} (\mathbb{C} : \mathbf{P}^a + \mathbf{W}^a \cdot \boldsymbol{\sigma} - \boldsymbol{\sigma} \cdot \mathbf{W}^a) : \mathbf{P}^b - \vartheta \Delta t \frac{\partial\dot{\gamma}^a}{\partial\tau_c^a} h_b^a \operatorname{sgn}(\dot{\gamma}(t)) \right]. \quad (2.98)$$

and $\{ \xi^a \}$ is the vector containing known quantities with the size given by the number of slip systems:

$$\{ \xi^a \} = \left\{ \Delta t \dot{\gamma}^a(t) + \vartheta \Delta t \frac{\partial\dot{\gamma}^a}{\partial\tau^a} (\mathbb{C} : \mathbf{P}^a + \mathbf{W}^a \cdot \boldsymbol{\sigma} - \boldsymbol{\sigma} \cdot \mathbf{W}^a) : \Delta\epsilon \right\}. \quad (2.99)$$

The solution for the slip increments is simply achieved by inverting the coefficient matrix:

$$\{ \Delta\gamma^b \} = [\mathbf{N}_b^a]^{-1} \{ \xi^a \}. \quad (2.100)$$

Once the slip increments are computed, the plastic velocity gradient in the intermediate configuration can also be computed using $\dot{\gamma}^a = \gamma^a/\Delta t$ and Eq. (2.14).

2.4.3. Material tangent

The material tangent is also derived for the forward-gradient case as explained in detail in Section 2.3.2. Differentiating the stress increment, $\Delta\sigma$ from Eq. (2.67), with respect to strain increment $\Delta\epsilon$ gives:

$$\frac{\partial\Delta\sigma}{\partial\Delta\epsilon} = \mathbb{C} - \frac{\partial}{\partial\Delta\epsilon} [\sigma \operatorname{tr}(\Delta\epsilon)] - \sum_a (\mathbb{C} : \mathbf{P}^a + \mathbf{W}^a \cdot \boldsymbol{\sigma} - \boldsymbol{\sigma} \cdot \mathbf{W}^a) \otimes \frac{\partial\Delta\gamma^a}{\partial\Delta\epsilon}. \quad (2.101)$$

Note that $\Delta\gamma^a$ and $\Delta\epsilon$ are related through the expression in Eq. (2.100), by differentiating we get:

$$\frac{\partial\Delta\gamma^b}{\partial\Delta\epsilon} = [\mathbf{N}_b^a]^{-1} \frac{\partial\xi^a}{\partial\Delta\epsilon}. \quad (2.102)$$

The term ξ^a is directly related to the total strain increment and differentiating (2.99):

$$\frac{\partial\xi^a}{\partial\Delta\epsilon} = \vartheta \Delta t \frac{\partial\dot{\gamma}^a}{\partial\tau^a} (\mathbb{C} : \mathbf{P}^a + \mathbf{W}^a \cdot \boldsymbol{\sigma} - \boldsymbol{\sigma} \cdot \mathbf{W}^a). \quad (2.103)$$

Substituting Eq. (2.103) to Eq. (2.102) gives the differential of the slip increments with respect to the total strain increments:

$$\frac{\partial\Delta\gamma^b}{\partial\Delta\epsilon} = \vartheta \Delta t \frac{\partial\dot{\gamma}^a}{\partial\tau^a} [\mathbf{N}_b^a]^{-1} \{ \mathbb{C} : \mathbf{P}^a + \mathbf{W}^a \cdot \boldsymbol{\sigma} - \boldsymbol{\sigma} \cdot \mathbf{W}^a \}. \quad (2.104)$$

Going back to (2.101) the Jacobian becomes:

$$\frac{\partial\Delta\sigma}{\partial\Delta\epsilon} = \mathbb{C} - \frac{\partial\Delta\sigma}{\partial\Delta\epsilon} \operatorname{tr}(\Delta\epsilon) - \sigma \frac{\partial\operatorname{tr}(\Delta\epsilon)}{\partial\Delta\epsilon} - \sum_a (\mathbb{C} : \mathbf{P}^a + \mathbf{W}^a \cdot \boldsymbol{\sigma} - \boldsymbol{\sigma} \cdot \mathbf{W}^a) \otimes \frac{\partial\Delta\gamma^a}{\partial\Delta\epsilon}. \quad (2.105)$$

Re-arranging terms gives:

$$\frac{\partial\Delta\sigma}{\partial\Delta\epsilon} [1 + \operatorname{tr}(\Delta\epsilon)] = \mathbb{C} - \sigma \frac{\partial\operatorname{tr}(\Delta\epsilon)}{\partial\Delta\epsilon} - \sum_a (\mathbb{C} : \mathbf{P}^a + \mathbf{W}^a \cdot \boldsymbol{\sigma} - \boldsymbol{\sigma} \cdot \mathbf{W}^a) \otimes \frac{\partial\Delta\gamma^a}{\partial\Delta\epsilon}. \quad (2.106)$$

The derivative of the trace of a second rank tensor is equal to the identity matrix, hence the Jacobian becomes:

$$\frac{\partial\Delta\sigma}{\partial\Delta\epsilon} [1 + \operatorname{tr}(\Delta\epsilon)] = \mathbb{C} - \sigma \otimes \mathbf{I} - \sum_a (\mathbb{C} : \mathbf{P}^a + \mathbf{W}^a \cdot \boldsymbol{\sigma} - \boldsymbol{\sigma} \cdot \mathbf{W}^a) \otimes \frac{\partial\Delta\gamma^a}{\partial\Delta\epsilon}. \quad (2.107)$$

in which the dyadic multiplication $\sigma \otimes I$ in direct notation is shown in Eq. (2.108) for clarity:

$$\sigma \otimes I = \begin{Bmatrix} \sigma_{11} \\ \sigma_{22} \\ \sigma_{33} \\ \sigma_{12} \\ \sigma_{13} \\ \sigma_{23} \end{Bmatrix} \left\{ \begin{array}{cccccc} 1 & 1 & 1 & 0 & 0 & 0 \end{array} \right\}. \quad (2.108)$$

The final expression for the material tangent is obtained by rearranging terms in Eq. (2.107) and substituting the expression for $\frac{\partial \Delta \gamma^a}{\partial \Delta \epsilon}$ from Eq. (2.104):

$$\left[\frac{\partial \Delta \sigma}{\partial \Delta \epsilon} \right] = \frac{\mathbb{C} - \sigma \otimes I - \sum_a (\mathbb{C} : P^a + W^a \cdot \sigma - \sigma \cdot W^a) \otimes \frac{\partial \Delta \gamma^a}{\partial \Delta \epsilon}}{1 + \text{tr}(\Delta \epsilon)}. \quad (2.109)$$

This material tangent provided an alternative solution based on the slip increments, which is more stable than the stress solver, Eq. (2.50). The tangent together with stress is the backup solution and they are used if the stress solver does not converge.

2.4.4. Fully-implicit method

The forward-gradient (linear) method explained in Section 2.4 was implemented in an iterative loop for consistent calculation of slip increments. In this case, the residual, Ψ , is formulated in terms of slip increments by substituting Eq. (2.95) into the residual (2.10):

$$\Psi = \Delta \gamma^a - (1 - \vartheta) \Delta t \dot{\gamma}^a(t) - \vartheta \Delta t \dot{\gamma}^a(\tau, \tau_c). \quad (2.110)$$

The solution of Eq. (2.110) is obtained by the Newton–Raphson scheme until each slip increment becomes less than the desired tolerance.

2.5. Plastic part of deformation gradient and orientation update

Once the crystal plasticity solution converges, important related quantities are computed. The plastic part of the deformation gradient is calculated using its value at the former time increment, $F_p(t)$, and L_p :

$$F_p = (I - L_p \Delta t)^{-1} F_p(t), \quad (2.111)$$

F_p is normalized by the cube root of its determinant such that the isochoric condition is maintained:

$$F_p = F_p / \sqrt[3]{\det(F_p)} \quad (2.112)$$

Stress is computed using its former value and the stress increment obtained by the solvers, Eq. (2.67) or Eq. (2.41):

$$\sigma = \sigma(t) + \Delta \sigma. \quad (2.113)$$

The orientations⁹ are updated using rotation rate, Ω_e , which is computed from the elastic spin increment according to Beausir et al. (2007):

$$\dot{g} = \Omega_e g. \quad (2.114)$$

Note that g is the current crystal orientation not the previous value $g(t)$. Adding the increment of orientation change gives the current orientation:

$$g = g(t) + \dot{g} \Delta t. \quad (2.115)$$

⁹ The rotation matrix g , is used to transform a vector in the crystal frame to the sample reference frame, while, g^T represents the conventional sample to crystal transformation. Both are passive transformations for the change of basis.

By substituting Eq. (2.114) into Eq. (2.115), utilizing the orthogonality of rotations, and rearranging the terms, we derive the equation to update the orientation:

$$g = (I - \Omega_e \Delta t)^T g(t). \quad (2.116)$$

For a given total rotation or spin, $\Delta \Omega$, which is prescribed by the total deformation, F , the elastic spin is computed by subtraction of the plastic spin from the total as in Eq. (2.117):

$$\Delta \Omega_e = \Delta \Omega - \Delta \Omega_p. \quad (2.117)$$

which is given in terms of the slip increments as in Eq. (2.118):

$$\Delta \Omega_p = \sum_a W^a \Delta \gamma^a. \quad (2.118)$$

The total spin increment can be computed from the velocity gradient according to Eq. (2.119):

$$\Delta \Omega = \frac{L - L^T}{2} \Delta t. \quad (2.119)$$

The plastic part of the deformation gradient and orientation update, once completed, are stored to be used as the former time values at the next time step.

2.6. Numerical scheme

Abaqus® user subroutines UMAT and UEXTERNALDB are used to implement the crystal plasticity solver available with open access (Tarleton, 2023). A UMAT subroutine is used to enter the user-defined material parameters for each element and integration point (IP) while a UEXTERNALDB subroutine is accessed externally once at the start of the analysis, at the beginning and end of a time increment for initialization. One-time initialization is performed at the beginning of the calculations for array allocation and assignment of mesh properties. Initialization at the IP level continues during the first increment to assign IP coordinates, material properties that can be different for each grain set;element, and to compute undeformed slip vector. Apart from that, initialization at the end of the first increment is needed to compute the gradient operators and volumes of each IP at the end of the first increment in the UMAT.

The crystal plasticity solver based on the Cauchy stress explained in Section 2.3 works as follows: for the nonlinear large deformation case Abaqus® gives the UMAT the current, F , and former, $F(t)$, total deformation gradients for a time step, Δt , between the displacement field increments. From these, the velocity gradient, L , is calculated using (2.8) which is then used to calculate the strain rate (2.9), spin (2.11), and the strain increment (2.10). The solution assumes that every related quantity that belongs to the former time step is stored and known. The elasticity matrix in the crystal reference is transformed to the deformed configuration using the crystal-to-sample transformation matrix with (2.27) which is later used to calculate the trial stress with (2.34) using the elastic strain increment at the previous time step. A guess of the stress is obtained either by the forward gradient method or using (2.43). Within the stress iteration algorithm, the stress is resolved to the slip systems with (2.38). The RSS is used with constitutive laws, either of the slips laws in (3.5), (3.12), or (3.13) to compute slip rates for the corresponding effective CRSS in (3.1). The slip rates are then summed to give the increase in plastic strain using (2.35), which allows the calculation of the residual in (2.33) and the tangent of the residual (2.36). The stress increment is then calculated using the Newton–Raphson scheme with (2.41). The stress is updated using (2.42) until its incremental change is less than a tolerance. Once the stress iteration converges, state increments are calculated using (2.45) for the corresponding slip increments explicitly in a single step or semi-implicitly within another loop using (2.46). Finally, other dependent quantities are updated, such as crystal orientation using (2.116), the plastic part of the deformation gradient with (2.111) and (2.112), and

Table 1

Model parameters used in the simulations unless otherwise stated.

C_{11}	C_{12}	C_{44}	b^a	τ_c^0	α	n	$\dot{\gamma}$	h_0	s_s	m	q	θ
170 GPa	124 GPa	75 GPa	2.56×10^{-4} μm	16 MPa	0.25	20	0.001 s^{-1}	250 MPa	190 MPa	2.5	1.4	298 K

the tangent stiffness matrix using (2.51). A similar method is used for the forward-gradient solution described in Section 2.4.

The numerical method is a unique mixture of the stress update method based on deformed vectors (Dunne et al., 2007) and a forward-gradient/fully-implicit solution technique based on slip increments (Huang, 1991). Fig. 2 shows the algorithm used in the crystal plasticity solver to minimize convergence issues and time cutbacks. The forward-gradient (FG) approach provides both an initial stress guess to the solver and a backup solution in case the stress iteration does not converge. Most convergence problems occur when inverting the $[\mathbb{I} + \mathcal{C} : \mathbb{P}]^{-1}$ matrix in Eq. (2.41), due to the large spectral range that occurs (near singular matrices) for higher slip rates calculated with exponential-based slip laws. Therefore, singular value decomposition (SVD) is added as an optional alternative approach to do the inversion by generalized pseudo-inverse. In addition, the CP solver has semi-implicit and fully-implicit state update procedures that deal with high-strain hardening/softening rates. Therefore, the hybrid methodology developed has the flexibility to deal with various convergence issues.

3. Results

The developed crystal plasticity-based finite element model was applied to simulate various cases to investigate the capability of the developed code. The widely accepted copper parameters were used; as shown in Table 1. These were used in the simulations unless otherwise specified. This study aims to provide information on the selection of model parameters by showing the sensitivity of stress on these parameters.

All the input files of the example cases in the following sections are included in the GitHub link: <https://github.com/TarletonGroup/CrystalPlasticity/tree/master/Examples>. The orientation calculations are based on the Bunge convention (Bunge, 2013), with the Euler angles expressed in degrees.

3.1. CRSS

The proposed framework has the flexibility to deal with different state variables for various strain-hardening and irradiation models and their effect on strength. The most general form of the effective CRSS, τ_{eff}^a , which considers the effect of all possible state variables on CRSS including lattice friction, τ_c^0 , Voce-type phenomenological hardening, τ_c^a , Taylor strength with geometric factor, α , forest dislocation, ρ_{for}^a , cut-through mechanism, and irradiation effects phenomenologically by solute strength, τ_s , or physically by defect loops of different types denoted by l with loop density, ρ_{loop}^l , and loop-slip strength interaction coefficients, J_l^a , (Note that some of the material models that cannot co-exist, i.e. irradiation model can be either model-1 or model-2 that will be explained in detail later):

$$\begin{aligned} \tau_{eff}^a = & \underbrace{\tau_c^0}_{\text{friction stress}} + \underbrace{\tau_c^a}_{\text{Voce hardening}} \\ & + Gb^a \sqrt{\underbrace{\alpha^2 \rho_{for}^a}_{\text{cut-through strength}} + \underbrace{\sum_l (J_l^a)^2 \rho_{loop}^l}_{\text{irrad. model-2}}} + \underbrace{\tau_s}_{\text{irrad. model-1}} \end{aligned} \quad (3.1)$$

Forest dislocations are computed using proper projections considering the statistically-stored dislocation (SSD) and the geometrically-necessary dislocation (GND) density of edge and screw dislocations

with line directions of t^b and s^b , respectively¹⁰:

$$\rho_{for}^a = \sum_b |\mathbf{n}^a \cdot \mathbf{t}^b| (\rho_{GND_e}^b + \rho_{SSD_e}^b) + |\mathbf{n}^a \cdot \mathbf{s}^b| (\rho_{GND_s}^b + \rho_{SSD_s}^b). \quad (3.2)$$

The edge and screw components of the SSD density ($\rho_{SSD_e}^a$ and $\rho_{SSD_s}^a$) are computed using an appropriate mapping χ . Square dislocation loops consisting of equal amounts of positive and negative edge and screw dislocations densities are assumed for SSDs. Therefore, χ is used to map these square loops in each slip system from the SSD density, ρ_{SSD}^b , to SSD edge and screw dislocation families:

$$\left\{ \begin{array}{l} \rho_{SSD_e}^a \\ \rho_{SSD_s}^a \end{array} \right\} = [\chi_b^a] \{ \rho_{SSD}^b \}. \quad (3.3)$$

The total density in a slip system is obtained by the sum of the SSD and GND densities:

$$\rho_{tot}^a = \sum_a \rho_{SSD}^a + |\rho_{GND_e}^a| + |\rho_{GND_s}^a|. \quad (3.4)$$

3.2. Slip laws

Three commonly used slip laws are implemented. Different slip models can co-exist for different materials or regions in the domain. We investigated the effect of the main parameters on the stress-strain response using a single crystal model along the cube orientation consisting of eight elements with unit dimensions loaded to 10% uniaxial tensile strain at a constant strain rate of 0.02 s^{-1} .

In the following sections, strain hardening effects were suspended to examine the effect of only slip parameters on flow stress. The parameters were investigated for a large spectrum of values showing the improved convergence response of the proposed model.

3.2.1. Thermally-activated slip (slip model-1)

Thermally-activated glide law governed by the hyperbolic-sine slip law is the original form of thermally activated glide that considers the probability of backward dislocation jumps as a function of resolved shear stress (RSS), τ^a , and backstress, X^a :

$$\dot{\tau}^a = A^a \sinh [B^a (|\tau^a - X^a| - \tau_{eff}^a)] \operatorname{sgn}(\tau^a - X^a), \quad \text{if } |\tau^a - X^a| - \tau_{eff}^a > 0. \quad (3.5)$$

Calculation of the parameter A^a is performed based on slip system quantities such as mobile dislocation density, ρ_m , vibration frequency of dislocations, v_0 , Boltzmann constant, k_B , temperature, θ , Helmholtz free energy, ΔF , that might be different for different slip families:

$$A^a = \rho_m (b^a)^2 v_0 \exp \left(-\frac{\Delta F^a}{k_B \theta} \right) \quad (3.6)$$

In the case of the presence of irradiation, in one of the models the fraction of mobile dislocations is altered by the factor, ψ , to account for the decrease in dislocation mobility:

$$\rho_m = \psi \rho_m^0 \quad (3.7)$$

The parameter B^a for a general case with state variables per slip system (indicated with the superscript a) reads:

$$B^a = \frac{\Delta V^a}{k_B \theta} \quad (3.8)$$

¹⁰ The line direction of an edge dislocation in slip system b , t^b , is obtained by the cross product of the slip direction, s^b , and slip plane normal, \mathbf{n}^b .

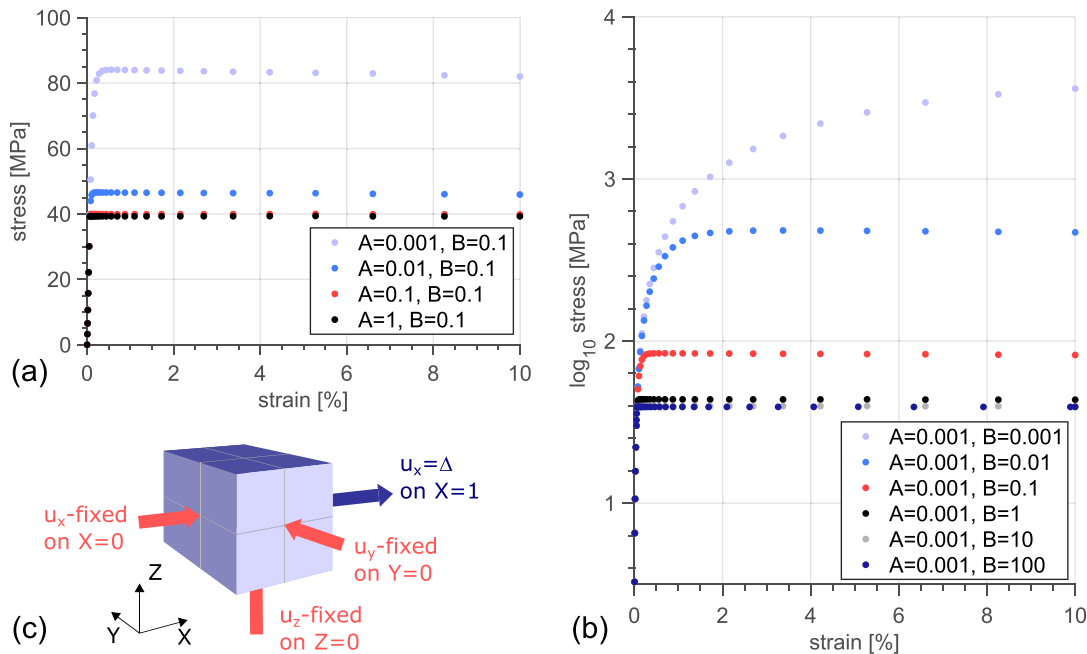


Fig. 3. Effect of the parameters of the hyperbolic-sine slip law (a) A [s^{-1}] and (b) B [MPa^{-1}].

The activation volume ΔV^a is computed by assuming it as a multiple of the volume governed by Burgers vector where ΔV_0 is a dimensionless factor:

$$\Delta V^a = \Delta V_0 (b^a)^3 \quad (3.9)$$

Alternatively, activation volume can also be defined as a multiple of the jump distance:

$$\Delta V^a = \lambda^a (b^a)^2 \quad (3.10)$$

In that case, the jump distance is set by the dislocation spacing:

$$\lambda^a = 1 / \sqrt{\rho_{for}^a} \quad (3.11)$$

The forest spacing leading to the variation in the activation volume causes potential convergence problems in using hyperbolic-sine slip law. The use of a simplified expression by defining the parameters A and B as constants helps to overcome this problem. Fig. 3 shows the stress-strain curves for different sets of parameters for A in the range $0.001\text{--}1.0 s^{-1}$ and B in the range $0.001\text{--}100.0 MPa^{-1}$. B parameter determines how sharp the transition to yield would be; thus, the sensitivity of the strain rate converges to the insensitive behavior of the rate as B increases. The yield point increases as A decreases, revealing a rate-sensitive behavior. This analysis shows the capability of the CP-solver to deal with a wide range of parameters that depend on intrinsic material properties.

3.2.2. Thermally-activated slip ignoring backward dislocation jumps (slip model-2)

A thermally-activated glide law is also available in a temperature-dependent exponential form by ignoring the probability of backward dislocation jumps. The slip model is capable of taking into account the long-range stress field (back stress), X^a . In this model, slip is a function of reference slip rate, $\dot{\gamma}_0$, and exponential constants p and q (that typically vary $0 \leq p \leq 1$ and $1 \leq p \leq 2$ characterizing the shape of the statistical obstacle profile (Follansbee and Kocks, 1988)):

$$\dot{\gamma}^a = \dot{\gamma}_0 \exp \left\{ -\frac{\Delta F}{k_B \theta} \left[1 - \left(\frac{|\tau^a - X^a|}{\tau_{eff}^a} \right)^p \right]^q \right\} \operatorname{sgn}(\tau^a - X^a). \quad (3.12)$$

Fig. 4 shows the effect of changing these parameters on the stress-strain response. $\dot{\gamma}_0^a$, p , and q all effect the yield point.

3.2.3. Power law (slip model-3)

Power law slip is the most common method to compute the slip rates using RSS as the driving force and CRSS as the threshold for slip as shown in Eq. (3.13) in which the $\dot{\gamma}_0$ and n represent the reference slip rate and rate-sensitivity exponent (Asaro, 1983), respectively:

$$\dot{\gamma}^a = \dot{\gamma}_0 \left(\frac{|\tau^a - X^a|}{\tau_{eff}^a} \right)^n \operatorname{sgn}(\tau^a - X^a). \quad (3.13)$$

Fig. 5 shows the effect of the reference slip rate, $\dot{\gamma}_0$, and the rate sensitivity exponent, n , on the stress-strain response. The flow stress is proportional to n , while inversely proportional to $\dot{\gamma}_0$. Decreasing the rate-sensitivity exponent eventually changes the yield transition from rate-dependent to perfectly plastic behavior.

3.2.4. Creep law (creep model-1)

The creep affects the slip rate by causing unpinning of dislocations which was found to be the governing mechanism for creep. Creep effects on slip is more pronounced than the axial strains and volumetric changes due to dislocation climb. Therefore, creep law defines the slip in terms of two contributions related to the creep (slip) and damage phenomenologically (Skamniotis et al., 2023):

$$\dot{\gamma}^a = \dot{\gamma}_C \exp \left(b_C |\tau^a - X^a| - \frac{Q_C}{R \theta} \right) \operatorname{sgn}(\tau^a - X^a) + \dot{\gamma}^a \dot{\gamma}_D \exp \left(b_D |\tau^a - X^a| - \frac{Q_D}{R \theta} \right) \operatorname{sgn}(\tau^a - X^a), \quad (3.14)$$

$$\dot{\gamma}^a = \int_0^t |\dot{\gamma}^a| dt. \quad (3.15)$$

The identical equation form applies to both creep deformation and damage. The parameters of the model governed by (3.14) include the stress multipliers b_C and b_D , as well as the activation energies Q_C and Q_D . The reference rates for creep and damage, indicated as $\dot{\gamma}_C$ and $\dot{\gamma}_D$, correspond to these phenomena. R and θ indicate the universal gas constant and temperature, respectively.

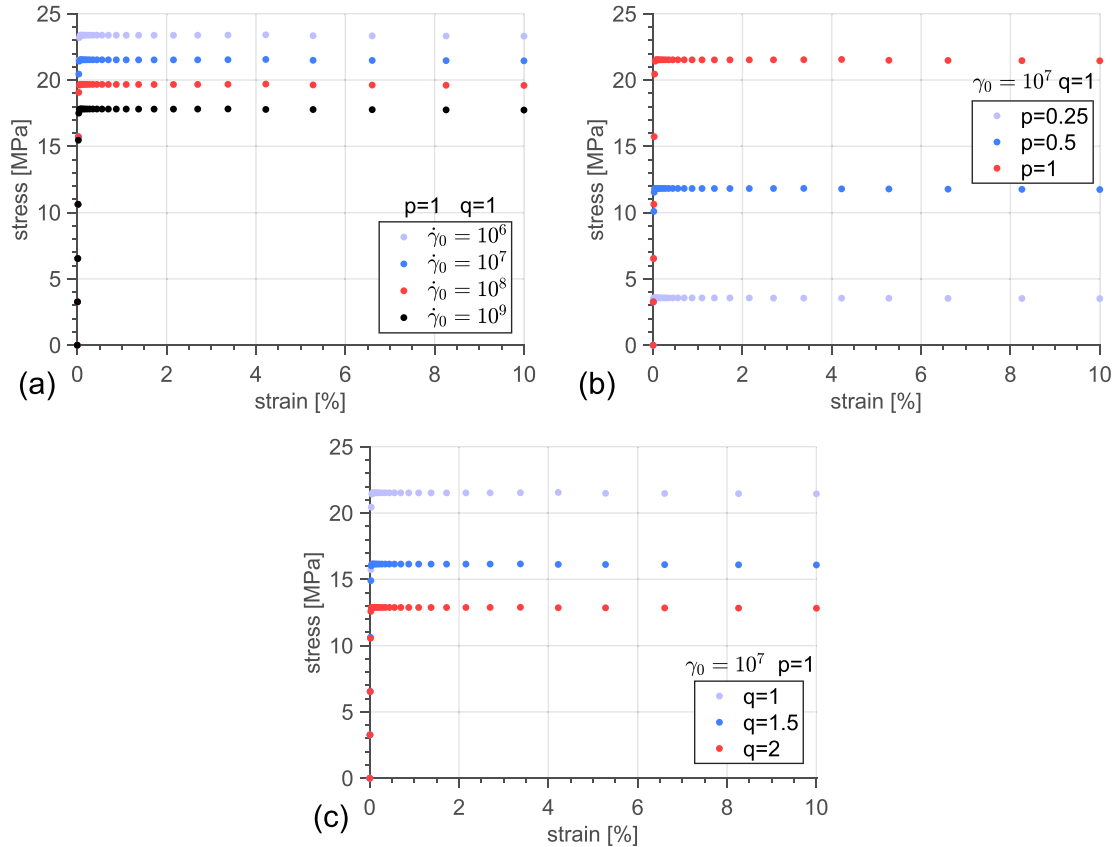


Fig. 4. Exponential slip law, affect of the: (a) reference slip rate, $\dot{\gamma}_0^a$ [s^{-1}], (b) exponent p [-], and (c) exponent q [-].

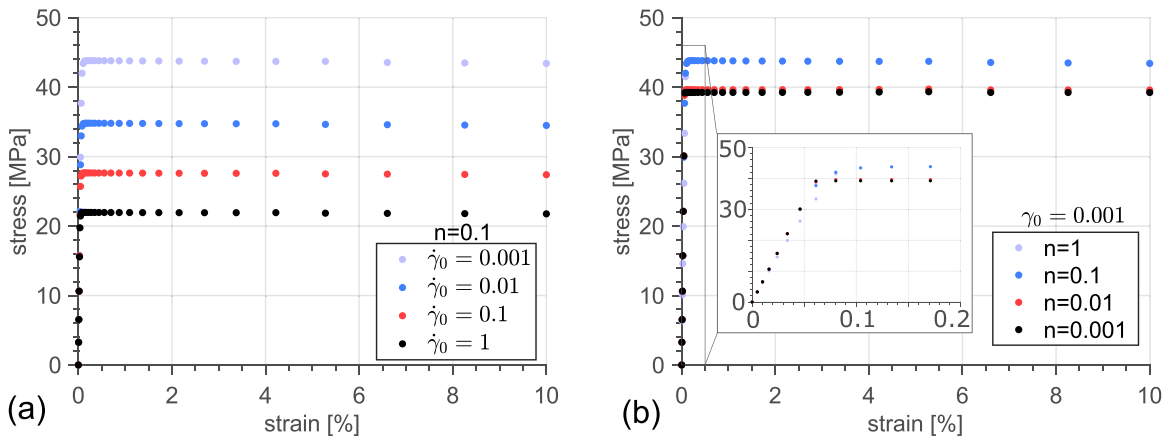


Fig. 5. Power law, the effect of the parameters (a) reference slip rate, $\dot{\gamma}_0^a$ [s^{-1}], for constant $n = 0.1$ [-] and (b) rate-sensitivity exponent, n [-], for constant $\dot{\gamma}_0 = 0.001$ [s^{-1}].

3.3. Strain hardening laws

Different strain hardening models are implemented, including models without hardening, Voce-type, linear, and Kocks-Mecking-Estrin models.

3.3.1. Voce-type (hardening model-1)

Voce-type hardening (Wagoner, 1980) is used to compute the self-strain hardening rate of a slip system in which h_0 , s_s , m prescribe hardening rate, saturation value of CRSS, and hardening exponent,

respectively (Values and units are shown in Table 1.).

$$\dot{h}^b = h_0 \left(1 - \frac{\tau_c^b}{s_s} \right)^m |\dot{\gamma}^b|, \quad (3.16)$$

The strain hardening interaction is considered by the latent hardening matrix:

$$\dot{\tau}_c^a = \sum_b H_b^a \dot{h}^b. \quad (3.17)$$

The hardening interaction matrix has unit values for coplanar systems, while a latent hardening constant greater than unity, q , is used for strain hardening in non-coplanar slip systems.

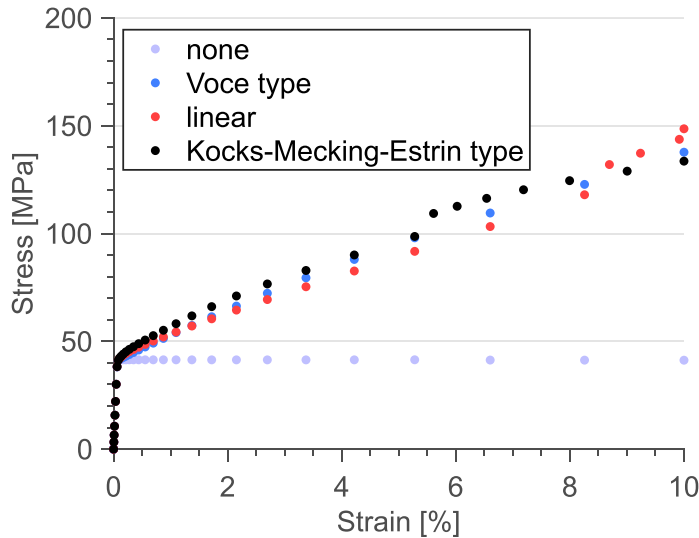


Fig. 6. Strain hardening response of none, linear, Voce, and Kocks-Mecking-Estrin hardening models.

Table 2
Hardening model parameters.

Voce-type	$h_0 = 250 \text{ MPa}$	$s_s = 190 \text{ MPa}$	$m = 2.5$	$q = 1.4$
linear	$k = 1550 \mu\text{m}$	$\varrho_{SSD}^0 = 1.8 \mu\text{m}^{-2}$		
KME type	$k_1 = 1466$	$k_2 = 200$	$\varrho_{SSD}^0 = 1.8 \mu\text{m}^{-2}$	

3.3.2. Linear dislocation evolution (hardening model-2)

The dislocation evolution per slip system is considered linearly proportional to the corresponding total slip in that slip system (Dunne et al., 2007):

$$\dot{\varrho}_{SSD}^a = k |\dot{\gamma}^a|. \quad (3.18)$$

3.3.3. Kocks–Mecking–Estrin (hardening model-3)

Kocks–Mecking–Estrin (KME) type hardening (Kocks and Mecking, 2003) has a hardening term inversely proportional to the forest spacing while the temperature and strain rate dependent annihilation term is linearly proportional to the dislocation density on the slip system:

$$\dot{\varrho}_{SSD}^a = \left(k_1 \frac{\sqrt{\varrho_{for}^a}}{b^a} - k_2(\dot{\epsilon}, \theta) \varrho_{SSD}^a \right) |\dot{\gamma}^a|. \quad (3.19)$$

We used a single crystal model loaded to 10% uniaxial tensile strain along a cube orientation consisting of eight elements at a strain rate of 0.02 s^{-1} . For no hardening, no evolution of state variables was allowed. The hardening parameters for the linear and KME hardening laws were obtained by trial-error until a reasonable match was obtained with the Voce-type hardening response. The strain hardening parameters are shown in Table 2 and the rest of the material parameters were the same as in Table 1.

Fig. 6 shows a comparison of available strain hardening models that were calibrated with respect to Voce-type law to obtain a comparable response approximately with an additional case of no strain hardening. The linear hardening model is limited to linear response and nonlinear hardening can be modeled using Voce or KME hardening laws. The observed slight jumps in the stress–strain response were due to the explicit state update used in the calculations.

3.4. Strain-gradient models

Strain gradients are expressed in terms of the geometrically necessary dislocation density (GND) to be included in the strength of single crystals (Busso et al., 2000). Simplified Taylor's equation, Eq. (3.20), was used to compute the CRSS instead of Eq. (3.1) ignoring the effect of statistical hardening effects. CRSS on slip system a (τ_c^a) was a function of τ_c^0 , α , G , b^a , and ϱ_{GND}^a that represent the lattice friction, geometric factor, shear modulus, Burgers vector, and GND density:

$$\tau_c^a = \tau_c^0 + \alpha G b^a \sqrt{\varrho_{GND}^a}. \quad (3.20)$$

Several methods using different incompatibility measures are available to compute GND density for various types of finite elements (Demir et al., 2024). The error in the incompatibility associated with the total forms in Sections 3.4.1 and 3.4.2 were calculated to be much less than that of both the rate form (Section 3.4.3) and the slip gradient (Section 3.4.4).

3.4.1. Total form restricted to the active slip systems (GND model-1)

The total form of incompatibility, $-(\nabla \times \mathbf{F}_p)^T$, is used. The GND densities for edge and screw components are characterized by the line direction, \mathbf{l}^a :

$$\mathbf{A} = -(\nabla \times \mathbf{F}_p)^T = \sum_a \varrho_{GND}^a b^a s^a \otimes \mathbf{l}^a. \quad (3.21)$$

3.4.2. Total form with flux correction (GND model-2)

Total form with area correction of $-(\nabla \times \mathbf{F}_p)^T \mathbf{F}_p^T$ is used to account for the configuration changes as recommended in Cermelli and Gurtin (2001):

$$\mathbf{A} = -(\nabla \times \mathbf{F}_p)^T \mathbf{F}_p^T = \sum_a \varrho_{GND}^a b^a s^a \otimes \mathbf{l}^a. \quad (3.22)$$

The GND density in both of the total forms (GND models 1 and 2) is obtained by singular value decomposition followed by inversion to obtain the densities. The solution is restricted to the active slip systems which is determined based on the value of the total slip γ^a of the slip system a :

$$[\mathbf{A}] = \sum_a \begin{cases} \varrho_{GND}^a b^a s^a \otimes \mathbf{l}^a, & \text{if } |\gamma^a| > 10^{-10}, \\ 0, & \text{otherwise.} \end{cases} \quad (3.23)$$

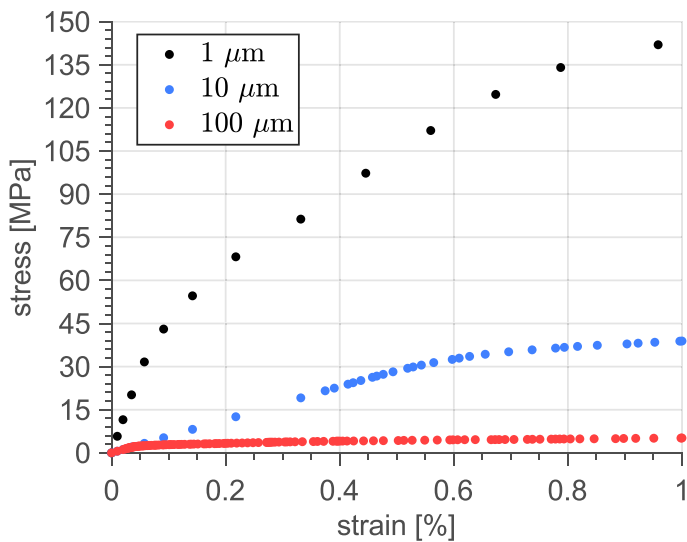


Fig. 7. Stress–strain response of single crystal cube cantilevered beam bending case for three different thicknesses of 1–10–100 μm . Euler angles of the beam were $(0^\circ, 0^\circ, 0^\circ)$.

3.4.3. Rate form for large deformations (GND model-3)

The rate form of $\nabla \times (\dot{\gamma}^a \mathbf{n}^a \mathbf{F}_p)$ can also be used in which the edge and screw dislocation families are calculated according to Eqs. (3.24) and (3.25), respectively:

$$\dot{\rho}_{GNDe}^a = -\frac{1}{b^a} \nabla \times (\dot{\gamma}^a \mathbf{n}^a \mathbf{F}_p) \cdot \mathbf{t}^a, \quad (3.24)$$

$$\dot{\rho}_{GNDs}^a = -\frac{1}{b^a} \nabla \times (\dot{\gamma}^a \mathbf{n}^a \mathbf{F}_p) \cdot \mathbf{s}^a. \quad (3.25)$$

The glissile jogs on edges that have their line direction along the slip plane normal are ignored in this study.

3.4.4. Rate form of slip gradient model (GND model-4)

Slip gradients for small deformations are used. The edge and screw dislocation densities are given by:

$$\dot{\rho}_{GNDe}^a = -\frac{1}{b^a} \nabla \dot{\gamma}^a \cdot \mathbf{s}^a, \quad (3.26)$$

$$\dot{\rho}_{GNDs}^a = \frac{1}{b^a} \nabla \dot{\gamma}^a \cdot \mathbf{t}^a. \quad (3.27)$$

In all GND models, an initial GND threshold is used to eliminate the artificial GNDs that are a result of small numerical differences between the slip at the integration points. These physically negligible GND densities tend to accumulate over time, hence they need to be eliminated using a threshold:

$$\rho_{GND}^a = \rho_{GND}^a(t) + \begin{cases} \Delta \rho_{GND}^a, & \text{if } |\Delta \rho_{GND}^a| > 2 \times 10^{-10} \mu\text{m}^{-2}, \\ 0, & \text{otherwise.} \end{cases} \quad (3.28)$$

A single crystal single slip case was studied to show the length scale effects. GND model-1 was used and the initial Euler angles of the beam were set in cube orientation $(0^\circ, 0^\circ, 0^\circ)$. The initial strength (τ_0^0) was set at 1 MPa to minimize the elastic effects. In this case study, no statistical hardening was used to demonstrate the effect of GNDs on hardening. The power law slip was applied utilizing the material parameters for copper listed in Table 1.

The effectiveness of the proposed length scale dependence model (GND model-1) was initially tested for the three different beam thicknesses of 1, 10, 100 μm . Linear hexahedral elements (C3D8) were used in this analysis, with five elements through the thickness and width directions and twenty-five elements through the length. The displacement was applied as a rotation boundary condition of 0.1 radians at

one end of the cantilevered beam, while the other end remained fixed for a total duration of 10 s.

Fig. 7 shows the resulting stress–strain response corresponding to cantilever beams of different thicknesses. The yield stress was the same for all thicknesses for the low initial CRSS value (1 MPa). The effect of strain hardening was pronounced as the thickness of the beam decreased. The cantilever beam was oriented so that bending can be achieved by a single slip. The initial Euler angles of the beam were $(-135^\circ, 35.264^\circ, -135^\circ)$ with respect to the sample reference to facilitate a single slip. The same model parameters were used for the investigation of the length-scale dependence. A linearly increasing moment of 1000 N μm was applied at one end of the beam for a duration of 10 s while the other end was fixed. Ten eight-node quadratic quadrilateral plane stress elements (CPS8) were used through the thickness and a hundred elements along the length of the beam.

The total slip was only along the first slip system with the $[1\bar{1}0]$ slip direction and the (111) slip plane. The slip in the other slip systems was negligible, Fig. 8. Therefore, single slip was achieved as desired.

The predicted GND density for the cantilever beam geometry was edge-type and on the first (active) slip system only. For this reason, the GND density on the remaining slip systems is expected to have negligible values. The restriction of the solution to the active slip systems led to vanishing GND density values on the other slip systems; see Fig. 9. The sign of the GND density was of the negative edge type, as expected for an ideal single slip case with positive bending moment (Arsenlis and Parks, 1999). In addition, there was no self-hardening due to the increase in the GND density, as the CRSS was only related to the forest density, Eq. (3.1). This shows the importance of this constraint regarding the complexity of strain hardening in case of the presence of the GND density on non-active slip systems that the L2-method would reveal (Arsenlis and Parks, 1999). The proposed SVD approach (GND model-1) is capable of dealing with single slip cases as the worst case because the dislocation tensor is in its most sparse form.

3.5. Back stress

In reverse loading of metals, a decrease in yield strength (Sowerby et al., 1979) followed by a stronger response to hardening under strain has been experimentally observed (Demir and Raabe, 2010). This kinematic hardening effect needs to be included for accurate modeling of metallic materials.

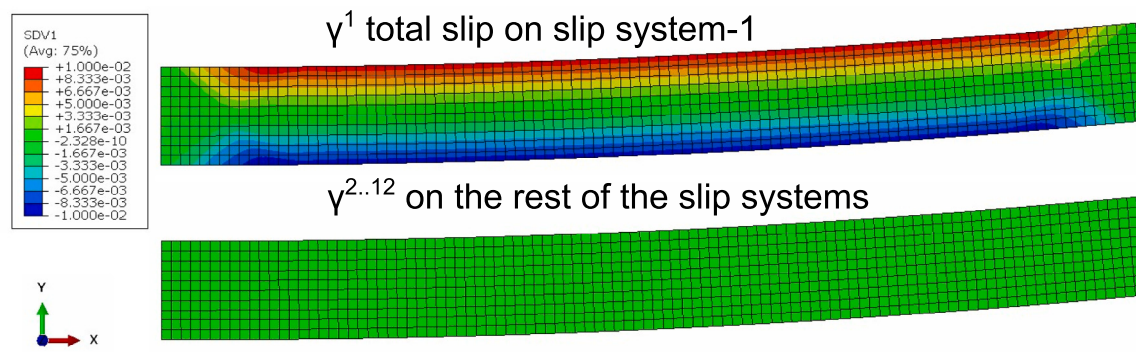


Fig. 8. Single crystal single slip bending case. Total slip, γ^a , distribution on the $[1\bar{1}0]$ (111) slip system and on all other systems. Euler angles of the beam were $(-135^\circ, 35.264^\circ, -135^\circ)$ to give a beam axis of $[1\bar{1}2]$.

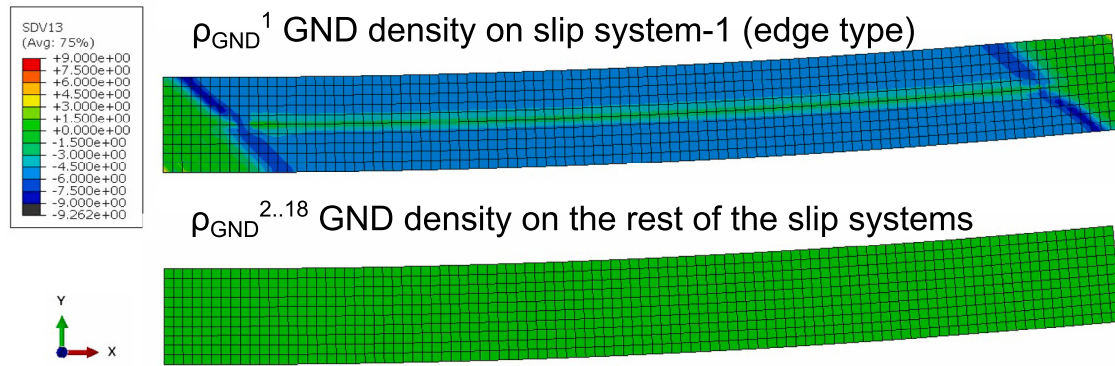


Fig. 9. The corresponding distribution of GND density, on the $[1\bar{1}0]$ (111) slip system and on all other systems. The total form of lattice incompatibility (GND model-1) was used in the simulations.

3.5.1. Armstrong–Frederick (back stress model-1)

A local Armstrong–Frederick (A–F) back stress model (Armstrong et al., 1966) is adopted and slightly modified for crystal plasticity with slip systems to incorporate back stress (Agius et al., 2020). The kinematic hardening term in slip constitutive laws Eqs. (3.5), (3.12), and (3.13), evolve linearly with slip, while the softening term has a bilinear dependence on slip and back stress. At saturation ($\dot{X}^a = 0$), the kinematic stress reaches a value of h/h_D :

$$\dot{X}^a = h \dot{\gamma}^a - h_D X^a |\dot{\gamma}^a|. \quad (3.29)$$

3.5.2. GND-based (back stress model-2)

A non-local GND-based back stress model was implemented that is similar to that previously reported (Kapoor et al., 2018; Bandyopadhyay et al., 2021) originally inspired by the experimental evidence of Slesewyk et al. (1978). Similar to the geometric factor α of CRSS in Eq. (3.1), ζ is used as a strength scaling factor :

$$X^a = \zeta b^a G \left(\frac{\sqrt{|\rho_{GND e}^a|}}{1-\nu} + \sqrt{|\rho_{GND s}^a|} \right) \operatorname{sgn}(\gamma^a). \quad (3.30)$$

We have used the sign of the total slip as a memory to store the sense of the polarization. To explain this, consider a single slip cantilever beam bending case. The shear stress has opposite signs on the above and below the neutral axis, GND density however has a single sign (negative edge for positive bending case with the positive slip direction aligned with the maximum stress direction). Therefore, the sign of the GND density does not represent the sign of the backstress that oppose the applied stress in a simple monotonic loading case. For this reason, the sign of total slip in Eq. (3.30) was used to account for the alteration of the sign of the back stress above and below the neutral axis of the beam.

The effects of back stress on a polycrystal RVE in a cube shape with an edge length of $40 \mu\text{m}$ were investigated. RVE was loaded to a displacement of $0.1 \mu\text{m}$ corresponding to 0.25% strain along the x direction in 10 s, followed by releasing the load for a duration of 1 s, and reverse loading for an absolute displacement of $0.1 \mu\text{m}$ that corresponds to -0.25% strain in 10 s. The parameters for the A–F model were $h = 6555 \text{ MPa}$ and $h_D = 245$ as kinematic hardening and softening parameters, respectively. The Voce-type strain hardening was present to investigate the actual conditions, including the effects of strain hardening and latent hardening. Similarly, the strength factor, ζ , was 0.25 for the non-local GND-based back stress model. The remaining parameters were the same as in Table 1.

Fig. 10(a) shows the stress vs. strain curves that are obtained by averaging the true strains (LE11) and the true stress (S11) of all the integration points in the RVE. Polycrystal RVE consisted of 34 grains and 64,000 elements.

Both the A–F and GND-based back stress models capture the two important features of the Bauschinger effect that was experimentally observed: i. drop in the flow stress upon reverse loading, and ii. change in the strain hardening response during reverse loading. Both models exhibit a clear drop in flow stress after reverse loading. The strain hardening for A–F is slightly altered. In contrast, the GND-based model had a lower strain hardening response in the reverse loading case, which is linked to the reduction of the GND density and the corresponding decrease in the CRSS. The yield point of both models is the same during forward loading. However, there is a significant strain hardening difference between the two models which is apparent in the forward loading curve, which is linked to the additional strengthening due to GND density. Further adjustment of the parameters with the

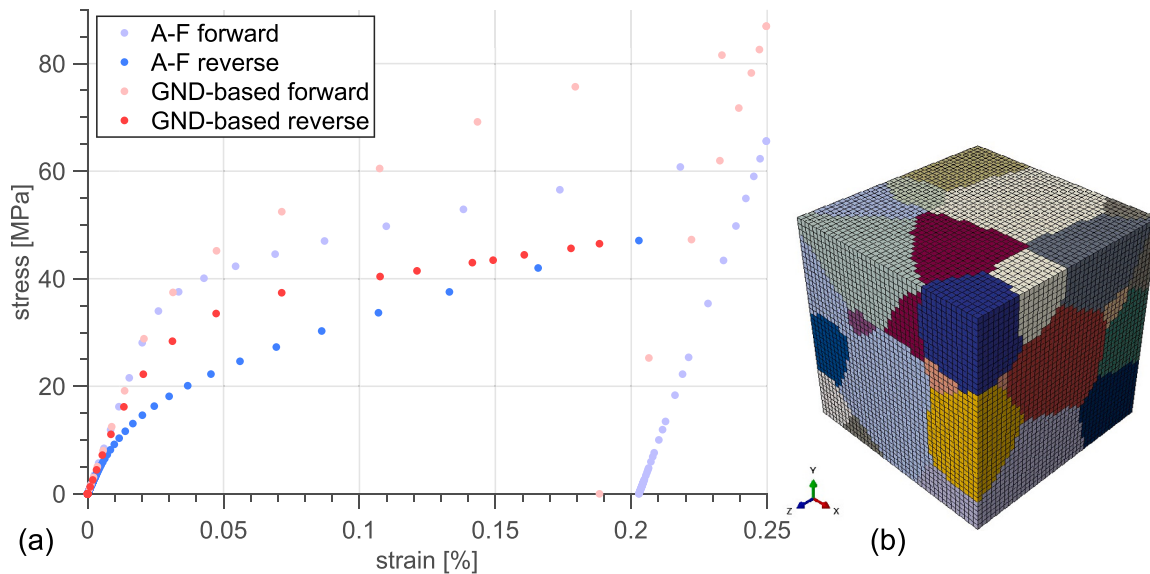


Fig. 10. (a) Average absolute value of stress vs. strain curves with two different back stress models during forward and reverse loading (curves are shifted to origin for comparison) and (b) polycrystal RVE used in the simulations (colors indicate grains).

Table 3
Slip and strain hardening parameters for irradiated zirconium (Hardie et al., 2022).

Parameter	Value	Unit
c/a	1.57	–
b ^{1–6}	3.2 × 10 ⁻⁴	μm
b ^{7–30}	6.0 × 10 ⁻⁴	μm
α	0.22364	–
ρ _{SSD} ⁰	10	μm ⁻²
E ₁	98.32	GPa
E ₃	123.28	GPa
G ₁₂	32.01	GPa
v ₁₂	0.4	–
v ₁₃	0.24	–
τ _c ^{1–3}	180.7	MPa
τ _c ^{4–6}	140.8	MPa
τ _c ^{7–12}	140.8	MPa
τ _c ^{13–24}	489.8	MPa
τ _c ^{25–30}	2449.1	MPa
ρ _{m0}	0.01	μm ⁻²
v ₀	10 ¹¹	s ⁻¹
ΔF	5 × 10 ⁻²⁰	J
ΔV ₀	20.93	μm ³
k	2600	μm ⁻²

experiments for the two back stress modeling approaches together with the experiments is needed.

3.6. Irradiation models

The material properties of zirconium (HCP) were used in the simulations, **Table 3**. The hyperbolic-sine slip with thermal activation parameters was used with linear dislocation evolution.

The irradiation effects were simulated on a single crystal. The model consisted of eight hexahedral elements with linear interpolation (C3D8), as shown in **Fig. 5(c)**. A tensile strain of 10% was applied along the X-direction for a duration of 10 s. Euler angles were (0°, 0°, 0°), and the loading axis was along one of the basal slip directions (X-axis).

3.6.1. Solute strength (irradiation model-1)

This is a simplified model to incorporate irradiation hardening effects using only three parameters. The irradiation effects are assumed to be isotropic, which means that the same level of influence of the

Table 4
Solute strength (irradiation model-1) parameters.

Parameter	Value	Unit
Γ _s	0.025	–
τ _s ⁰	75	MPa
ψ	3.457 × 10 ⁻²	–

irradiation-induced defects is considered uniformly in all slip systems. The effect of irradiation is considered by an additional strength that is referred to as the solute strength, τ_s :

$$\tau_s = \tau_s^0 \exp\left(-\frac{\Gamma_s}{\Gamma_s}\right). \quad (3.31)$$

in which τ_s^0 and Γ_s represent the initial value of the solute strength and the amount of cumulative slip required for softening. The irradiation strength degrades exponentially with cumulative slip.

A secondary effect of irradiation is the reduction in the mobile dislocation density that enters the coefficient, A^a , that is used for thermally activated slip, Eq. (3.6). This was considered by taking a constant fraction, ψ , of the mobile dislocation density of an un-irradiated material, ρ_m^0 :

$$\rho_m = \psi \rho_m^0 \quad (3.32)$$

Table 4 shows the model parameters used in this study for zirconium in conjunction with the model parameters shown in **Table 3**.

3.6.2. Loop defects (irradiation model-2)

This model takes into account the irradiation-induced defects in the form of dislocation loops (Hardie et al., 2022). These ‘a-type’ loop defects have their habit planes determined based on experimental observations. For example, for zirconium, the defects were along the three typical $\langle a \rangle$ directions: $[2\bar{1}\bar{1}0]$, $[\bar{1}\bar{1}20]$, and $[2\bar{1}\bar{1}0]$ which correspond to the slip directions of the fourth, sixth and eleventh slip systems E.6, respectively.

To find the affect of irradiation on slip, the interaction between defects and slip needs to be quantified. First, the defect directions, s^l , were summed up with the slip direction of concern, s^a , to obtain the reaction product, r_l^a :

$$r_l^a = s^l + s^a \quad (3.33)$$

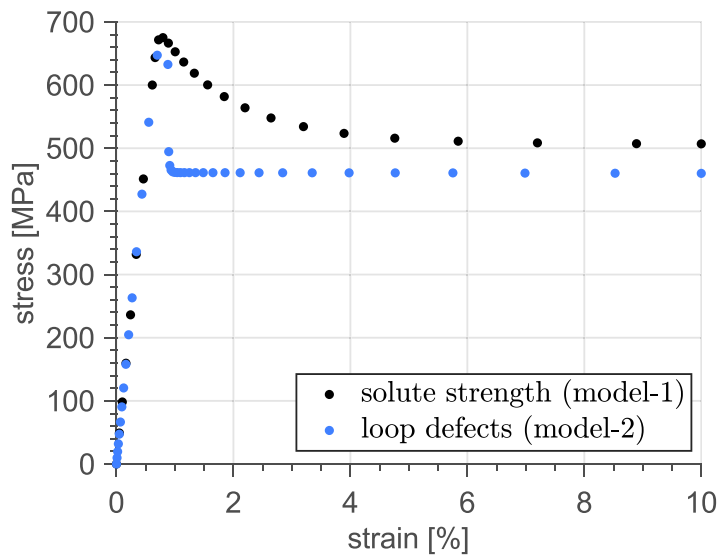


Fig. 11. Stress–strain curves for irradiated hardening models. Euler angles were $(0^\circ, 0^\circ, 0^\circ)$. The hcp crystal is loaded along the basal slip direction up to 10% strain for a duration of 10 s.

Table 5
Parameters for irradiated zirconium.

j_1	j_2	i_1	i_2	N_{loop}^0	d_{loop}^0
1.25	1.875	0.5	0.0	$2.033 \times 10^4 \text{ } \mu\text{m}^{-3}$	$1.4 \times 10^{-3} \text{ } \mu\text{m}$

Second, the reaction vector in Eq. (3.33) was then projected on the slip plane normal to get the scalar parameter, c_l^a , between the slip system a and the defect system l :

$$c_l^a = \mathbf{r}_l^a \cdot \mathbf{n}^a \quad (3.34)$$

Finally, the interaction matrix for strength in (3.1), J_l^a was computed by using two interaction parameters: j_1 and j_2 based on whether the value of the projection, c_l^a that has zero or non-zero magnitude:

$$J_l^a = \begin{cases} J_l^a = j_1, & \text{if } c_l^a = 0, \\ J_l^a = j_2, & \text{otherwise.} \end{cases} \quad (3.35)$$

and similarly the interaction matrix for strain-softening, I_l^a , was computed considering c_l^a having a magnitude of zero or non-zero:

$$I_l^a = \begin{cases} I_l^a = i_1, & \text{if } c_l^a = 0, \\ I_l^a = i_2, & \text{otherwise.} \end{cases} \quad (3.36)$$

in which j_1 , j_2 , i_1 , and i_2 are the strength and strain-softening interaction coefficients when $c_l^a = 0$ or otherwise.

The irradiation slip resistance reads Eq. (3.1) in which the density of the loop defects was computed using the number density of dislocation loops per unit volume, N^l , and the average diameter of these loops, d^l where the superscript l indicates the defect family:

$$\phi_{loop}^l = N^l d^l \quad (3.37)$$

The evolution of loop density is governed by considering the softening interactions between the slip systems and defects I_l^a represents the softening (hardening) interactions between the defects and slip systems:

$$\dot{\phi}_{loop}^l = \sum_a I_l^a \sqrt{\phi_{loop}^l} \frac{|\dot{\gamma}^a|}{b^a} \quad (3.38)$$

The effect of defect loops on the CRSS was computed considering the interactions between the loop defects and slip systems that are accounted for by the J_l^a matrix. Strength interactions enter through Eq. (3.19).

Table 5 shows the parameters of the irradiation hardening model used in this study. The resulting stress–strain curve shown in Fig. 11 exhibits an initial strengthening followed by softening. The model allowed for the incorporation of irradiation effects using a physical basis that is based on experimental observations.

3.7. Single crystal goss compression

Single crystal Goss compression tests were performed to simulate a cylinder with a circular cross-section becoming an ellipse due to plastic anisotropy. The model parameters were the same as shown in Table 1. Euler angles were $(45^\circ, 0^\circ, 0^\circ)$ with respect to the sample axes shown in Fig. 12.

Fig. 12(a) and (b) shows the transition of the circular cross section to an ellipse as in Kalidindi and Anand (1993). The strain hardening response was also the same as in the experimental curve in Kalidindi and Anand (1993). The calculation efficiency tends to increase the time steps and the explicit default state update causes the jumps in the stresses. These jumps disappear when semi-implicit or fully implicit state update was used. This study validates the correct incorporation of the plastic anisotropy of slip and the consistency of the proposed solver.

3.8. Single crystal copper tension

Copper single crystal experiments of Takeuchi (1975) was used to benchmark simulations. Tensile simulations were along the crystallographic directions of $\langle 001 \rangle$, $\langle 101 \rangle$, $\langle 112 \rangle$, and $\langle 111 \rangle$ that correspond to the Euler angles of $(0^\circ, 0^\circ, 0^\circ)$, $(180^\circ, 45^\circ, 0^\circ)$, $(0^\circ, 54.3^\circ, 45^\circ)$, and $(-90^\circ, 35.2644^\circ, 45^\circ)$, respectively. The finite element model has 45 mm long with a displacement of 9 mm applied along the z-direction corresponding to the engineering strain 20%. The degrees of freedom at the ends of the sample along the x and y directions are fixed to represent the clamped boundary conditions in the experiments shown in Fig. 13(b).

The KME hardening was used as in (3.19) and calibration was performed only for the $\langle 001 \rangle$ tensile data. The same value of parameters was used for each crystallographic direction for consistency as shown in Table 6. The different initial value of the yield in the experiments suggests the presence of a difference in the CRSS due to the initial dislocation density, for example, for the experimental result for the

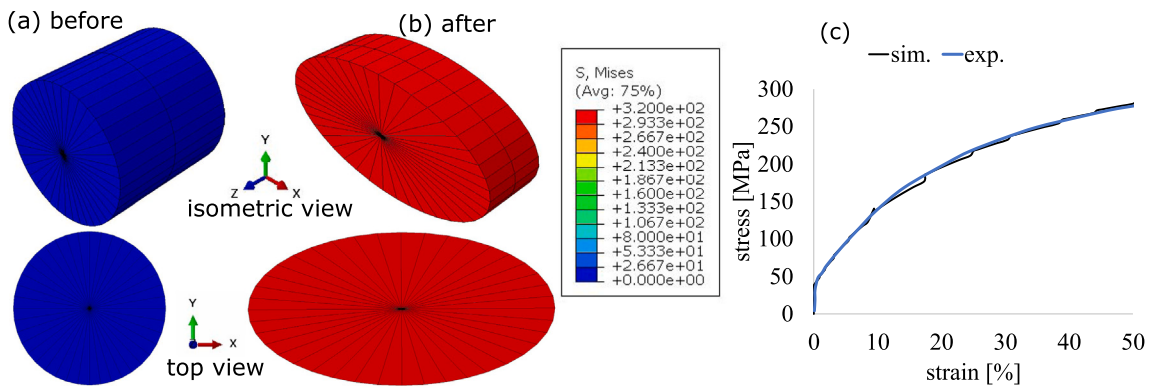


Fig. 12. Single crystal Goss compression (a) von Mises stress before deformation, (b) von Mises stress after 70% strain, and (c) stress–strain curve. Euler angles were ($45^\circ, 0^\circ, 0^\circ$). Experimental data is for copper from [Kalidindi and Anand \(1993\)](#).

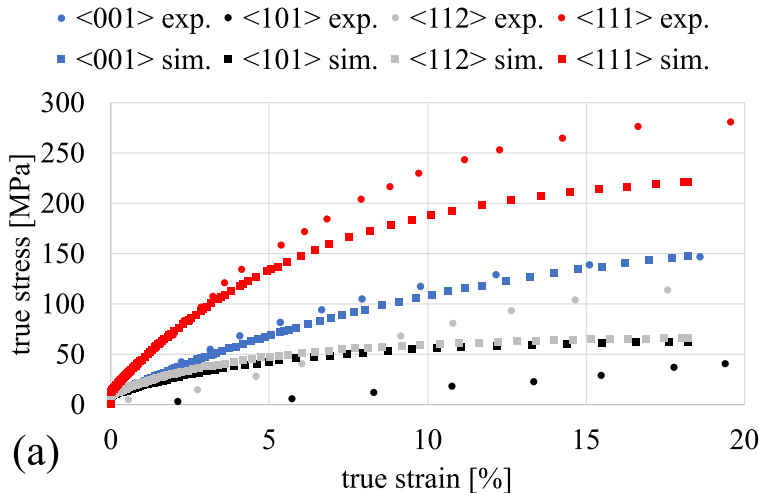


Fig. 13. Single crystal copper tensile response (a) true stress vs. true strain, (b) finite element model. Tensile strain of 20% was applied along the z-axis with a strain rate of $3 \times 10^{-3} \text{ s}^{-1}$.

Table 6

Model parameters used in the single crystal tension simulations for the KME hardening model. τ_c^0 : lattice friction, ρ_{SSD}^0 : initial SSD density, k_1 : mean-free-path hardening factor, k_2 : annihilation coefficient, α : geometric factor. The remaining parameters are the same as in [Table 1](#).

τ_c^0	ρ_{SSD}^0	k_1	k_2	α
1 MPa	$0.05 \mu\text{m}^{-2}$	0.0625	50	$0.25/\sqrt{2}$

$\langle 101 \rangle$ direction. These experimental differences were neglected in the simulations, and the same values were used for all model parameters.

[Fig. 13\(a\)](#) illustrates the comparison between the stress-strain responses. Despite the discrepancies between the simulated and experimental curves, the simulation aligns closely with the experimental data. A key aspect of this study is the incorporation of the sum of total and forest densities, similar to parallel and forest density, as described in Gottstein's work ([Gottstein, 2004](#)). Prior to this adjustment, the single-crystal curves exhibited a mixed order with the crystallographic direction. Thus, the effective CRSS is redefined in (3.1) as:

$$\tau_{eff}^a = \tau_c^0 + \alpha G b^a \sqrt{\rho_{for}^a + \rho_{tot}^a} \quad (3.39)$$

The total and forest dislocation densities are obtained using Eqs. (3.2) and (3.4), respectively.

3.9. Polycrystal simulations

The RVE resolution and size has been shown to play a central role in macro- and micro-scale stress responses ([Kanit et al., 2003](#)). Polycrystal RVE was generated using Dream3D® with an average grain size of $24.5 \mu\text{m}$ (natural logarithm of average grain size, $\mu=3.2$) and with a standard deviation of $2.7 \mu\text{m}$ (natural logarithm of standard deviation of average grain size, $\sigma=1$). The minimum and maximum cut-off values were set to give minimum and maximum feature sizes of $4.1 \mu\text{m}$ and $25.8 \mu\text{m}$, respectively, to allow the presence of a range of grain sizes within the cube-shaped RVE, resulting in 34 grains for an edge length of $40 \mu\text{m}$.

The resolution of the RVE was investigated by changing the resolution without altering the microstructure (e.g. crystallographic and morphological texture) by keeping the orientation and shape of each grain constant for a uniaxial tension of 2.5% axial strain. [Fig. 14](#) shows the resulting RVE for a range of resolutions (element sizes from $8 \mu\text{m}$ to $0.25 \mu\text{m}$) that were investigated with the corresponding total number of elements ranging from 125 to 4,096,000.

[Fig. 15](#) shows the influence of the RVE resolution on the macroscopic stresses. Macroscopic stresses converge after $2 \mu\text{m}$ resolution, which is approximately one fifth of the grain size, or approximately 625 elements per grain to have a converged macroscopic engineering stress and von Mises stress response. Convergence refers to the convergence of a finite element solution due to a numerical solution ideally converging with an infinite number of elements.

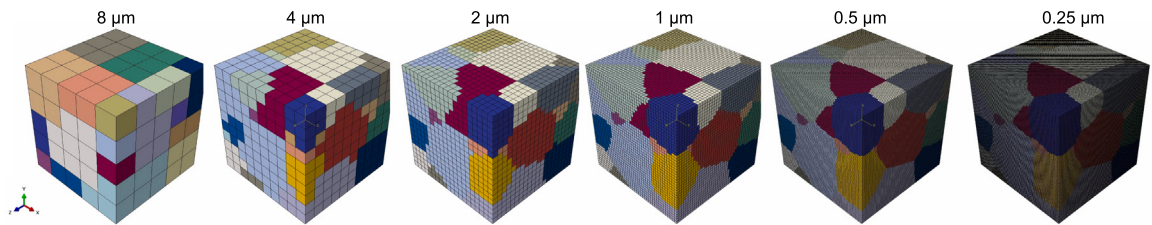


Fig. 14. A polycrystal RVE with a size of 40 μm size and $24.5 \pm 2.7 \mu\text{m}$ average grain size for a range of RVE resolutions (voxel sizes from 8 μm – 0.25 μm) generated using Dream3D[®]. Colors indicate grains and, at low resolutions, small grains disappear due to coarse resolution, resulting in a different color code.

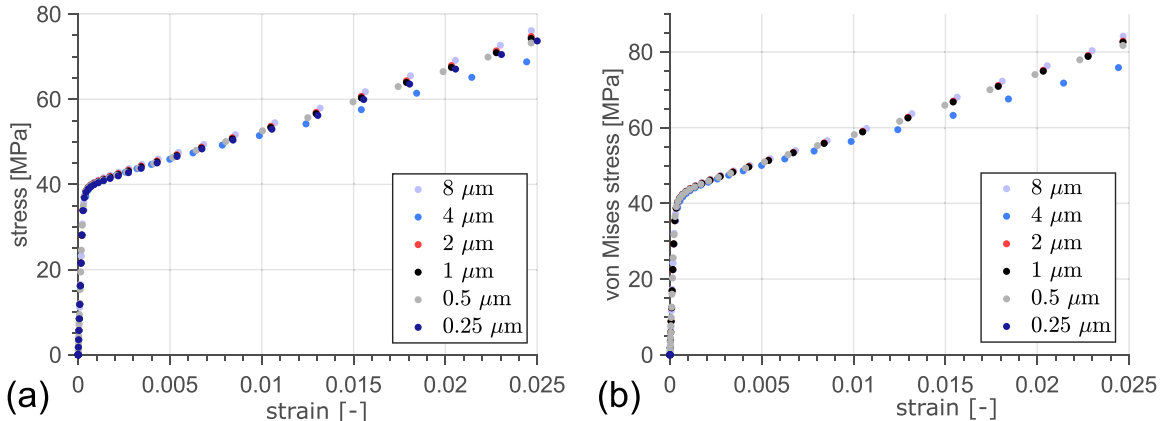


Fig. 15. Macroscopic scale stresses obtained by averaging over the RVE: (a) engineering stress (S_{11}) and (b) von Mises stress (Mises) as a function of the RVE resolution.

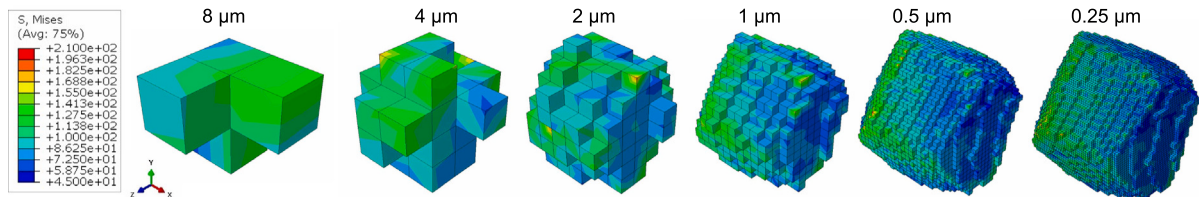


Fig. 16. Von Mises stress distributions on grain-18 in the middle of the RVE for different resolutions.

Fig. 16 shows the distribution of the microscale stresses in the mid-grain (grain-18). Microscale distributions start to resemble each other below the resolution of 1 μm indicating the greater mesh refinement necessary for microscale convergence than for the macroscale convergence. The voxel size is approximately one-tenth of the average grain size, or ten elements per edge of a grain, demanding approximately a thousand elements per grain for convergence.

3.10. Element type

Tetrahedral meshes can be preferred over hexahedral elements due to their superior meshing capabilities. However, it is well known that linear tetrahedrals may suffer from shear locking and they are much stiffer than the quadratic tetrahedral and hexahedral type elements. To investigate the effect of element type on mechanical response at the macro- and microscales, the same polycrystal RVE was simulated using quadratic tetrahedral (C3D10) and linear hexahedral (C3D8) elements with full integration for a uniaxial tension load case.

Polycrystal RVEs were generated using NEPER[®] with a size of 1 μm edge length consisting of 30 grains, **Fig. 17(a)**. The hexahedral mesh had 27 elements per edge to make a total element number of 19,683, while the tetrahedral mesh had a non-uniform spacing on average of 13 elements per edge consisting of 24,012 elements. Although the mesh grids were different, the mesh refinement parameter used to

generate the RVE was the same for both cases. The number of elements for a tetrahedral mesh increase 3/2 times more than a hexahedral mesh for the same level of mesh refinement. The grain boundaries are represented as continuous lines for a Voronoi tessellation by tetrahedral elements instead of the saw-tooth representation of grain boundaries by uniform grid of hexahedral elements. Tensile loading up to 25% strain was applied over 10 s in time along the X-direction. The material properties are shown in [Table 1](#).

The stress-strain curves and distributions both revealed a slightly stiffer engineering stress and a von Mises stress behavior with the quadratic tetrahedral elements, **Fig. 17(b)**. However, this can be attributed to the coarser mesh refinement of the tetrahedral elements. **Figs. 17(c) and (d)** show the total slip distribution on the deformed mesh. The deformed surface topologies match qualitatively, which justifies the use of both element types. In addition, the total slip distributions for the two cases were quite similar exhibiting a noticeable shear banding behavior for both element types. However, the local differences were greater when tetrahedral elements were used, indicating the presence of the smoothing effect of these local differences in the linear hexahedral elements because of their reduced ability to represent deformations involving high curvature.

Tetrahedral elements can offer a more realistic representation of grain boundaries. This is especially important for polycrystals involving fracture and damage that can initiate when stress is usually localized near the grain boundaries ([Quay et al., 2011](#)).

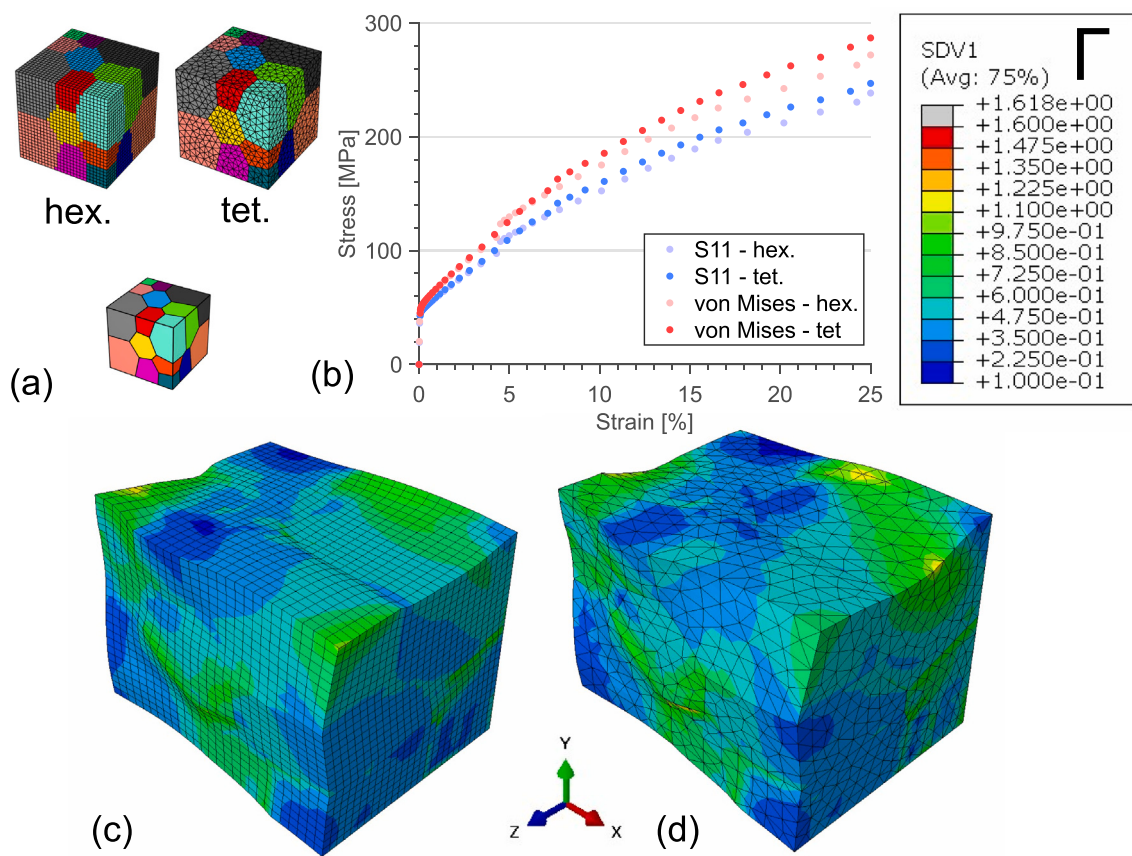


Fig. 17. Effect of element type: (a) Tessellation and mesh generation using NEPER®, (b) stress–strain response, total slip distributions on the RVE for (c) hexahedral and for (d) tetrahedral elements.

3.11. Time integration and state update techniques

We investigated the effect of the state update procedure on the computational time and the total number of time increments necessary for a polycrystal RVE containing six grains. A coarse grained polycrystal was selected to impose high stress gradients across grains, thus making convergence difficult. 10% uniaxial strain was applied in a time of 100 s. The material properties in Table 1 were used. The state update procedures can be linear (using the linear non-iterative solution in Peirce et al., 1982) explicit (the states belong to the former time), semi-implicit (the states belong to the current time obtained by a Euler time integration procedure as described in Kalidindi et al., 1992), or fully implicit (the states belong to current time that is simultaneously computed with the slip increments as described in Huang, 1991).

The linear solution refers to the forward-gradient method which is the linearized noniterative solution for the slip increments as described in Section 2.4. Therefore, the slip and strain hardening can be nonlinear. The OXFORD-UMAT linear solution reveals approximately 70% less computational time compared to the OXFORD-UMAT semi-implicit solution. The linear scheme works well if the very first strain increment is within the elastic limit of the material. Even though using the solver alongside the linear solution extends the overall simulation duration, having the linear solver as a backup during simulations of extensive polycrystal applications significantly reduces computational time in case a convergence issue arise.

The implicit state updates reveal a smoother stress–strain response free of the stress jumps in exchange for an additional increase of 133% and 454% in the computational time, respectively. The semi-implicit

state update in this case offers a stable solution free of jumps in the stress–strain curves with an acceptable decrease in the simulation time.

3.12. Comparison to the other crystal plasticity solvers

The performance of CP-based solver (OXFORD-UMAT) was compared to different CP UMAT subroutines that use Abaqus® as the same finite element software. The same field solver was used to compare other CP-based solvers to avoid complications related to differences in the FE solver and solution techniques. CP-based solvers use different time integration schemes. The OXFORD-UMAT is based on a hybrid scheme consisting of a crystal plasticity solver based on Cauchy stress and a forward-gradient scheme as described in detail in Section 2.4. UMAT (Huang, 1991) uses Huang's integration method, which was also formulated on the basis of the deformed vectors, and the primary variable is the slip increments. BRISTOL (Demir et al., 2023) used a time integration scheme that was formulated in the intermediate configuration using the 2nd Piola–Kirchoff stress as the primary variable.

The simulations were performed using the same material properties in Table 1 except the hardening exponent, m and the latent hardening parameter, q , which were set to unit values. Linear hardening was used because the UMAT (Huang, 1991) used a hyperbolic-secant type hardening rule without the hardening exponent, which was the reason for the slight difference in the stress–strain curves in Fig. 19(b). Similarly, UMAT (Huang, 1991) applies the latent hardening parameter to all slip systems except the self-slip system, while the others employ a latent hardening coefficient to the noncoplanar slip systems only, and hence

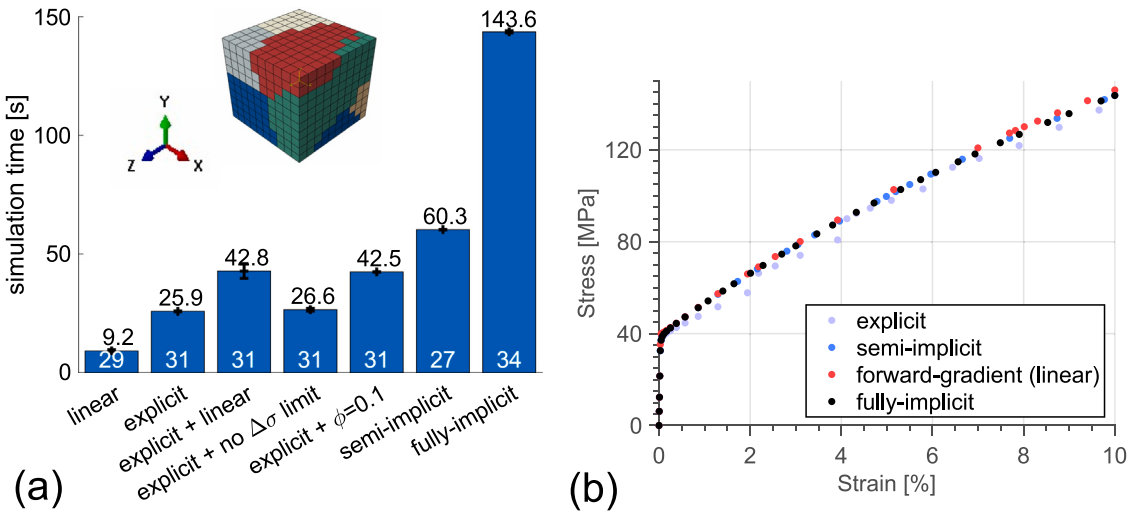


Fig. 18. Comparison of time integration and state update methods using OXFORD-UMAT: (a) simulation time (total number of time increments are indicated with white color.) and (b) engineering stress (S_{11}) vs. strain curves. The polycrystal RVE contains six grains. The stress based solver has explicit or semi-implicit state update procedures, while the slip-based solver can provide a linear (forward gradient) or a fully-implicit solution.

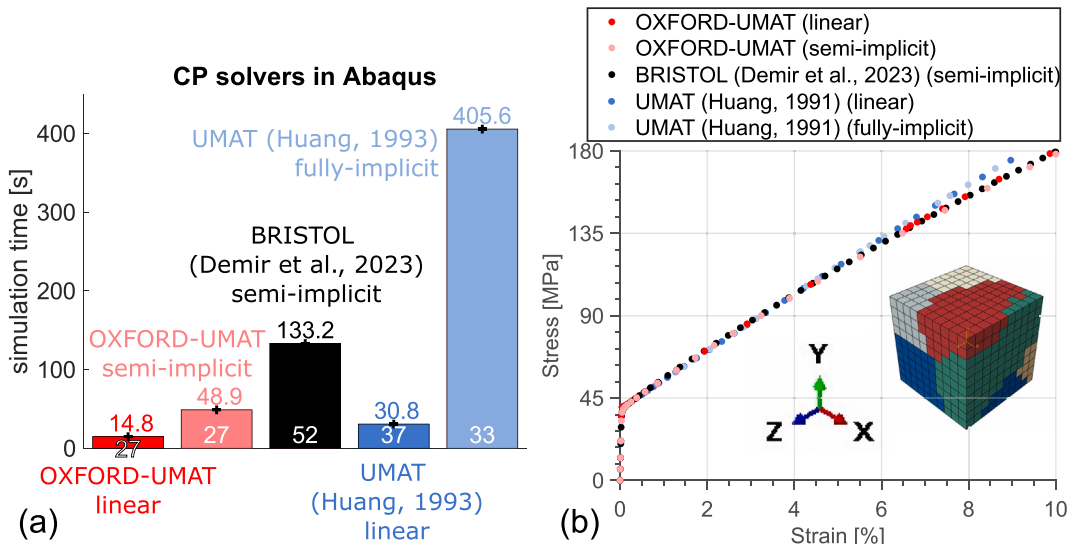


Fig. 19. Comparison of different solvers: (a) simulation time and (b) engineering stress (S_{11}) vs. strain curves. UMAT (Huang, 1991) and BRISTOL (Demir et al., 2023) are completely different solvers that work in Abaqus® which rely on forward-gradient (Asaro and Needleman, 1985) and Kalidindi-Anand (Kalidindi et al., 1992) time integration schemes, respectively. A polycrystal RVE consisting of 6 grains was investigated. Simulation time was computed by excluding the time required for initialization for all schemes.

to provide a reliable comparison, the latent hardening was set to unity for all slip systems. The von Mises stress distributions were quite similar to those obtained by entirely different solvers, showing the validity of the OXFORD-UMAT, Fig. 20.

The OXFORD-UMAT offers a range of solution options to select the level of efficiency depending on the application. The simplicity of the scheme resulted in lower computational times than that of both BRISTOL and UMAT (Huang, 1991) solvers. BRISTOL uses a different time-stepping method that is explained in Kalidindi et al. (1992) which leads to a greater number of time increments (52 time steps) than the others. In addition, BRISTOL (Demir et al., 2023) takes into account changes in the slip vectors implicitly considering a more complex residual that leads to a complicated tangent for the Newton-Raphson iteration. Similarly, the tangent stiffness is computed using a rigorous seven-step method (Lieou and Bronkhorst, 2020; Zhang et al., 2021; Demir et al., 2023). UMAT (Huang, 1991) has a fully-implicit scheme

that is slower than both OXFORD-UMAT and BRISTOL (Demir et al., 2023), which may be linked with the presence of the hyperbolic-secant strain hardening rule.

3.13. Miscellaneous

In this section, the influence of the initial guess and the stress increment correction on the solution efficiency is investigated. The model parameters as shown in Table 1 were used with the nonlinear slip rule and strain hardening, including the effect of latent hardening.

We have found a significant affect of the initial guess on the convergence rate and therefore on the computational time according to Hardie et al. (2023). The initial guess was calculated using the weighted average of the fully elastic and fully plastic guesses using a factor ϕ in this study. Approximately 40% gain (nearly one half) in computational time was obtained as the initial guess approaches the

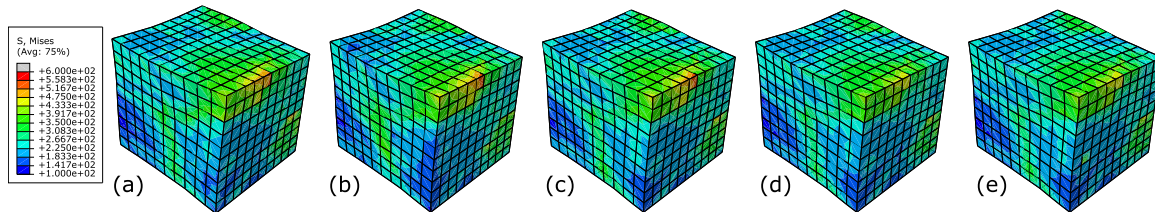


Fig. 20. Von Mises stress distribution (MPa) at the end of 10% tensile strain: (a) UMAT-OXFORD (linear), (b) UMAT-OXFORD (semi-implicit), (c) BRISTOL (semi-implicit) (Demir et al., 2023), (d) UMAT (linear) (Huang, 1991), and (e) UMAT (fully-implicit) (Huang, 1991).

fully plastic guess rather than using 0.1 as the weight for a fully elastic guess ($\phi = 0.1$), Fig. 18(a).

Correction of large stress increments exceeding a tolerance $f \tau_c$ in Eq. (2.43) as used in Kalidindi et al. (1992), helps the convergence significantly. This correction regarding the large stress increments allows the crystal plasticity iteration to converge faster and continue with large time steps without the time cutbacks, thereby leading to an efficient solution. The comparison of an explicit scheme with that correction and without; which is referred to as the ‘explicit + no $\Delta\sigma$ limit’ case in Fig. 18, shows approximately 10% reduction in computational time. Therefore, we have this minor correction in Eq. (2.43) can help reduce the number of time increments.

The solution considering the stress threshold and with fully plastic initial guess was set as the two default settings of the CP-based solver. The linear solution can be used as a predictor and a backup solution in case convergence fails, acknowledging the likelihood of significant errors associated with the explicit solution for a highly nonlinear problem that causes convergence failure in the first place.

The proposed method has the option of deciding the factor to push the time increment. It is usual practice to use 1.25 as the magnitude of that factor. However, our experience with a variety of problems suggests leaving the time-stepping decision to the field solver. Therefore, we found that it would be a better practice to let Abaqus® decide on the time increment considering various other factors while leaving the option to the user.

4. Conclusions

In this study, a crystal plasticity framework (OXFORD-UMAT) is developed and implemented in a finite element framework. The framework has constitutive laws to account for temperature dependence, slip, creep, strain hardening, length-scale dependence, back stress, and irradiation effects. The model is tested against Goss compression, uniaxial tension and polycrystal cases, and it can deal with extreme material properties and parameters leading to almost rate-insensitive behavior. The comparison of models with existing crystal plasticity solvers reveals the validity and relative computational efficiency that can be attained with the simplicity of the OXFORD-UMAT framework. Several modifications have led to significant time savings. For example, the use of i. fully plastic guess (40%), ii. a threshold for stress increase (10%), iii. linear solver (70%). The crystal plasticity solver is available for public access in a modular form that allows other researchers to use and develop constitutive models easily (Tarleton, 2023). In summary, the computational efficiency together with multiple solver structure makes OXFORD-UMAT a versatile alternative for crystal plasticity applications.

CRediT authorship contribution statement

Eralp Demir: Writing – review & editing, Writing – original draft, Software, Methodology, Data curation, Conceptualization. **Alvaro Martinez-Pechero:** Writing – review & editing, Data

curation. **Chris Hardie:** Writing – review & editing, Funding acquisition. **Edmund Tarleton:** Writing – review & editing, Supervision, Methodology, Funding acquisition.

Declaration of competing interest

The authors declare the following financial interests/personal relationships which may be considered as potential competing interests: Edmund Tarleton reports financial support was provided by Royal Academy of Engineering. Chris Hardie reports financial support was provided by UKAEA. If there are other authors, they declare that they have no known competing financial interests or personal relationships that could have appeared to influence the work reported in this paper.

Acknowledgments

We greatly appreciate the discussions with Professor Fionn Dunne on the models developed in this study. A. M. Pechero acknowledges the support of the EPSRC, United Kingdom Energy Programme [grant number EP/W006839/1]. E. Tarleton acknowledges financial support from the Royal Academy of Engineering and the UK Atomic Energy Authority (UKAEA), United Kingdom through a Senior Research Fellowship. The authors appreciate the user time provided by Advanced Research Computing at the University of Oxford (ARC-Oxford) to perform the large-scale polycrystal simulations carried out within this study. We also acknowledge the STEP funding program of the UKAEA.

Appendix A. Code inputs

PROPS vector is the property entry of Abaqus® that contains at least six mandatory entries while 300 optional entries that correspond to material properties. The mandatory entries are Euler angles (ϕ_1, Φ, ϕ_2) in the Bunge convention (Bunge, 2013) and in degrees as PROPS(1-3), an integer grain ID as PROPS(4), and an integer material ID as PROPS(5). The rest of the inputs are decided using PROPS(6) by either of the following:

1. PROPS(6) = 1: Read the material properties from PROPS vector of a length of 300, or,
2. PROPS(6) = 0: Read the corresponding material parameters from the ‘usermaterials.f’ file for the corresponding material ID identified in PROPS(5). The total length of the PROPS vector is 6 in this case.

The other important entries are the total number of elements in the mesh, the type of elements, and the maximum number of slip systems that are defined in the ‘userinputs.f’ file. The same file also contains the input parameters related with the numerical solution, the type of the solver(s), non-local GND calculation method, and the type of the back stress model.

The in-grain orientation scatter can be included in the model through a ‘*.vox’ file that has a default format such that the rows

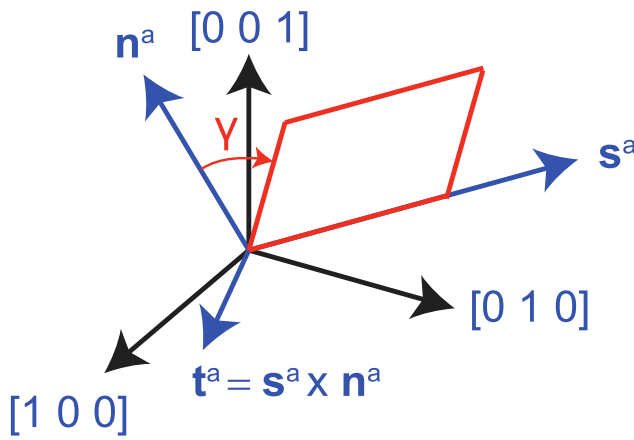


Fig. C.1. Slip as a simple shear type of deformation (red color) in slip the reference a (blue color) and crystal reference (black color).

correspond to $\phi_1, \Phi, \phi_2, x, y, z$, grain-id, and phase-id for each element. The filename and folder location shall be indicated in ‘**userinputs.f**’ file.

Appendix B. Code outputs

The important state variables can be visually outputted using state-dependent variables (SDV) in the DEPVAR function of Abaqus®. The number of outputs may take a significant amount of disk space; thus, the decision of the outputs is left as optional in the ‘**useroutputs.f**’ file. In this case, the number of state-dependent variables (SDV) that are defined in the model shall match or be greater than the total number of outputs.

Appendix C. Schmid tensor

Slip is in the form of simple shear, as shown in Fig. C.1, hence the strain in the slip reference, ϵ^a :

$$\epsilon^a = \begin{bmatrix} 0 & \gamma & 0 \\ 0 & 0 & 0 \\ 0 & 0 & 0 \end{bmatrix}. \quad (\text{C.1})$$

The transformation from slip reference to crystal reference in Fig. C.1 is given by Eq. (C.2):

$$\mathbf{g}^{a2c} = [\ s^a \ n^a \ t^a]. \quad (\text{C.2})$$

Therefore, \mathbf{g}^{a2c} transforms the slip strain in the slip reference to the crystal reference. The strain is a second rank tensor hence transformation must be applied twice. Using index notation the slip in crystal transforms with Eq. (C.3):

$$\epsilon_{ij}^c = g_{im}^{a2c} g_{jn}^{a2c} \epsilon_{mn}^a. \quad (\text{C.3})$$

Since there is only ϵ_{12}^a term, Eq. (C.4) can be concluded:

$$\epsilon_{ij}^c = g_{i1}^{a2c} g_{j2}^{a2c} \epsilon_{12}^a. \quad (\text{C.4})$$

Note that the columns of the transformation are indeed slip vectors:

$$g_{i1}^{a2c} = s_i^a. \quad (\text{C.5})$$

$$g_{j2}^{a2c} = n_j^a. \quad (\text{C.6})$$

Substituting these identities to Eq. (C.4) with $\epsilon_{12}^a = \gamma$, the transformation becomes:

$$\epsilon_{ij}^c = s_i^a n_j^a \gamma. \quad (\text{C.7})$$

$s_i^a n_j^a$ represents the dyadic product of the slip direction and slip plane normal vectors which gives the Schmid tensor, Eq. (C.8):

$$S_{ij}^a = s_i^a n_j^a = S^a = s^a \otimes n^a. \quad (\text{C.8})$$

Therefore, Schmid tensor is the transformation required to find the corresponding strain at the in the crystal reference due to slip in a slip system.

Appendix D. Rate of change of slip direction and slip plane normal

The time rate of Eq. (2.68) and using chain rule gives the rate of change of RSS which involves time derivatives of slip direction and slip plane normal:

$$\dot{\tau}^a = \dot{s}_e^a \cdot \sigma \cdot n_e^a + s_e^a \cdot \dot{\sigma} \cdot n_e^a + s_e^a \cdot \sigma \cdot \dot{n}_e^a. \quad (\text{D.1})$$

Derivation of \dot{s}^a :

The deformed slip direction is computed using Eq. (D.2):

$$s_e^a = F_e s^a. \quad (\text{D.2})$$

The time rate of change of slip direction is given by Eq. (D.3) since the time rate of change of constant undeformed vectors is zero:

$$\dot{s}_e^a = \dot{F}_e s^a. \quad (\text{D.3})$$

Inversion of Eq. (D.2) gives:

$$s^a = F_e^{-1} s_e^a. \quad (\text{D.4})$$

Substituting the expression for s^a by using Eq. (D.4) into Eq. (D.3) gives:

$$\dot{s}_e^a = \dot{F}_e F_e^{-1} s_e^a. \quad (\text{D.5})$$

Using the property in Eq. (2.7), the elastic part of the velocity gradient can be found as in Eq. (D.6). In some Khan and Huang (1995) the elastic stretch part is neglected to give the elastic spin instead.

$$\dot{s}_e^a = \mathbf{L}_e s_e^a. \quad (\text{D.6})$$

Derivation of \dot{n}^a :

The slip plane normal is mapped with Eq. (2.17). Rewriting reads:

$$n_e^a = n^a F_e^{-1}. \quad (\text{D.7})$$

Taking time derivative of Eq. (D.7) gives:

$$\dot{n}_e^a = n^a \dot{F}_e^{-1}. \quad (\text{D.8})$$

Using properties for the derivative of inverse¹¹ reveals:

$$\dot{n}_e^a = -n^a F_e^{-1} \dot{F}_e F_e^{-1}. \quad (\text{D.9})$$

Also taking the inverse of Eq. (D.7) giving:

$$n^a = n_e^a F_e. \quad (\text{D.10})$$

Substituting Eq. (D.10) to Eq. (D.9) reads:

$$\dot{n}_e^a = -n_e^a F_e F_e^{-1} \dot{F}_e F_e^{-1}. \quad (\text{D.11})$$

which simplifies to:

$$\dot{n}_e^a = -n_e^a \dot{F}_e F_e^{-1}. \quad (\text{D.12})$$

or by using the identity in Eq. (2.7) becomes as Eq. (D.13):

$$\dot{n}_e^a = -n_e^a \mathbf{L}_e. \quad (\text{D.13})$$

¹¹ Differentiating the expression: $\mathbf{A} \mathbf{A}^{-1} = \mathbf{I}$, gives: $\partial \mathbf{A} \mathbf{A}^{-1} + \mathbf{A} \partial \mathbf{A}^{-1} = \mathbf{0}$ and by re-arranging terms the relation for the differential for the inverse can be obtained as: $\partial \mathbf{A}^{-1} = -\mathbf{A}^{-1} \partial \mathbf{A} \mathbf{A}^{-1}$.

Table E.1
Slip systems for BCC material (1–12).

s_c^α	[111]	[1̄1̄1]	[11̄1]	[1̄1̄1]	[111]	[1̄1̄1]	[1̄1̄1]	[11̄1]	[1̄1̄1]	[11̄1]	[1̄1̄1]
n_c^α	(110)	(110)	(101)	(101)	(1̄10)	(1̄10)	(1̄10)	(01̄1)	(01̄1)	(011)	(101)

Table E.2
Slip systems for BCC material (13–24).

s_c^α	[11̄1]	[1̄1̄1]	[1̄1̄1]	[111]	[1̄1̄1]	[11̄1]	[111]	[1̄1̄1]	[1̄1̄1]	[111]	[1̄1̄1]
n_c^α	(112)	(1̄12)	(1̄12)	(11̄2)	(121)	(1̄21)	(1̄21)	(12̄1)	(211)	(2̄11)	(21̄1)

Table E.3
Slip systems for FCC material (1–12).

n_c^α	(111)			(1̄1̄1)			(1̄1̄1)			(11̄1)		
	[11̄0]	[01̄1]	[10̄1]	[110]	[01̄1]	[101]	[110]	[011]	[10̄1]	[1̄10]	[011]	[101]

Table E.4
Slip systems for FCC material - for cubic slip (13–18).

sys.	s_c^α	n_c^α
13	[011]	(100)
14	[01̄1]	(100)
15	[101]	(010)
16	[10̄1]	(010)
17	[110]	(001)
18	[1̄10]	(001)

Table E.5
Slip systems for BCT material (1–8) with unit lattice dimensions indicated with the letters a, b, c.

sys.	s_c^α	n_c^α
1	[1 0 0]	(0 1 0)
2	[1 0 0]	(0 0 1)
3	[a ̄b 0]	(b a 0)
4	[a b 0]	(b ̄a 0)
5	[a ̄b 2c]	(0 c b/2)
6	[̄a b 2c]	(0 c b/2)
7	[a b 2c]	(0 c ̄b/2)
8	[a ̄b 2c]	(0 c ̄b/2)

Appendix E. Slip systems

The slip systems for the crystal structures of BCC, FCC, HCP, and BCT correspond to phases 1–2–3–4 (see Tables E.1–E.5). .

Data availability

The code and examples used in this paper are available with public access at <https://github.com/TarletonGroup/CrystalPlasticity>.

Table E.6

Slip systems for HCP material - for cubic slip (1–30) in Miller-Bravais indices. The hcp slip direction and slip plane normals converted to rectangular cartesian system by using equations $[uvw] \rightarrow [3u/2(u+2v) * \sqrt{3}/2w * (c/a)]$ and $(hkil) \rightarrow (h(h+2k)/\sqrt{3}l/(c/a))$, respectively.

System	Type	$s_c^\alpha_{(uvw)}$	$n_c^\alpha_{(hkil)}$
1	basal	[21̄10]	(0001)
2	basal	[12̄10]	(0001)
3	basal	[1̄120]	(0001)
4	prismatic	[21̄10]	(01̄10)
5	prismatic	[12̄10]	(̄1010)
6	prismatic	[1̄120]	(1̄100)
7	1st order pyramidal <a>	[12̄10]	(101̄1)
8	1st order pyramidal <a>	[21̄10]	(01̄11)
9	1st order pyramidal <a>	[1̄120]	(̄1101)
10	1st order pyramidal <a>	[12̄10]	(̄1011)
11	1st order pyramidal <a>	[21̄10]	(01̄11)
12	1st order pyramidal <a>	[1120]	(1̄101)
13	1st order pyramidal <c+a>	[21̄13]	(101̄1)
14	1st order pyramidal <c+a>	[1̄123]	(101̄1)
15	1st order pyramidal <c+a>	[1̄123]	(01̄11)
16	1st order pyramidal <c+a>	[12̄13]	(01̄11)
17	1st order pyramidal <c+a>	[1̄213]	(̄1101)
18	1st order pyramidal <c+a>	[21̄13]	(̄1011)
19	1st order pyramidal <c+a>	[21̄13]	(̄1011)
20	1st order pyramidal <c+a>	[1123]	(1011)
21	1st order pyramidal <c+a>	[1123]	(01̄11)
22	1st order pyramidal <c+a>	[12̄13]	(01̄11)
23	1st order pyramidal <c+a>	[12̄13]	(1̄101)
24	1st order pyramidal <c+a>	[21̄13]	(1̄101)
25	2nd order pyramidal <c+a>	[1̄123]	(11̄22)
26	2nd order pyramidal <c+a>	[12̄13]	(12̄12)
27	2nd order pyramidal <c+a>	[21̄13]	(21̄12)
28	2nd order pyramidal <c+a>	[1123]	(1̄122)
29	2nd order pyramidal <c+a>	[12̄13]	(12̄12)
30	2nd order pyramidal <c+a>	[21̄13]	(21̄12)

References

- Agius, D., Al Mamun, A., Simpson, C.A., Truman, C., Wang, Y., Mostafavi, M., Knowles, D., 2020. Microstructure-informed, predictive crystal plasticity finite element model of fatigue-dwells. Comput. Mater. Sci. 183, 109823.
- Armstrong, P.J., Frederick, C., et al., 1966. A mathematical representation of the multiaxial Bauschinger effect, vol. 731, Berkeley Nuclear Laboratories Berkeley, CA.
- Arsenlis, A., Parks, D., 1999. Crystallographic aspects of geometrically-necessary and statistically-stored dislocation density. Acta Mater. 47 (5), 1597–1611.
- Asaro, R.J., 1983. Crystal plasticity. J. Appl. Mech. 50 (4b), 921–934. <http://dx.doi.org/10.1115/1.3167205>.
- Asaro, R.J., Needleman, A., 1985. Overview no. 42 texture development and strain hardening in rate dependent polycrystals. Acta Metall. 33 (6), 923–953.

- Balasubramanian, S., 1998. Polycrystalline plasticity: application to deformation processing of lightweight metals (Ph.D. thesis). Massachusetts Institute of Technology.
- Bandyopadhyay, R., Gustafson, S.E., Kapoor, K., Naragani, D., Pagan, D.C., Sangid, M.D., 2021. Comparative assessment of backstress models using high-energy X-ray diffraction microscopy experiments and crystal plasticity finite element simulations. *Int. J. Plast.* 136, 102887.
- Barbe, F., Decker, L., Jeulin, D., Cailletaud, G., 2001a. Intergranular and intragranular behavior of polycrystalline aggregates. part 1: FE model. *Int. J. Plast.* 17 (4), 513–536.
- Barbe, F., Forest, S., Cailletaud, G., 2001b. Intergranular and intragranular behavior of polycrystalline aggregates. part 2: Results. *Int. J. Plast.* 17 (4), 537–563.
- Beausir, B., Tóth, L.S., Neale, K.W., 2007. Ideal orientations and persistence characteristics of hexagonal close packed crystals in simple shear. *Acta Mater.* 55 (8), 2695–2705.
- Bond, W.L., 1943. The mathematics of the physical properties of crystals. *Bell Syst. Tech. J.* 22 (1), 1–72.
- Bunge, H.-J., 2013. Texture analysis in materials science: mathematical methods. Elsevier.
- Busso, E.P., Cailletaud, G., 2005. On the selection of active slip systems in crystal plasticity. *Int. J. Plast.* 21 (11), 2212–2231.
- Busso, E., Meissonnier, F., O'dowd, N., 2000. Gradient-dependent deformation of two-phase single crystals. *J. Mech. Phys. Solids* 48 (11), 2333–2361.
- Cermelli, P., Gurtin, M.E., 2001. On the characterization of geometrically necessary dislocations in finite plasticity. *J. Mech. Phys. Solids* 49 (7), 1539–1568.
- Chen, J., Wang, Z., Korsunsky, A.M., 2022. Multiscale stress and strain statistics in the deformation of polycrystalline alloys. *Int. J. Plast.* 152, 103260.
- Cuitino, A.M., Ortiz, M., 1993. Computational modelling of single crystals. *Modelling Simul. Mater. Sci. Eng.* 1 (3), 225.
- Dawson, P.R., 2000. Computational crystal plasticity. *Int. J. Solids Struct.* 37 (1–2), 115–130.
- Dawson, P.R., Boyce, D.E., 2015. FEPX-finite element polycrystals: Theory, finite element formulation, numerical implementation and illustrative examples. arXiv preprint arXiv:1504.03296.
- Demir, E., Gutierrez-Urrutia, I., 2021. Investigation of strain hardening near grain boundaries of an aluminum oligocrystal: Experiments and crystal based finite element method. *Int. J. Plast.* 136, 102898.
- Demir, E., Horton, E.W., Mokhtarishirazabad, M., Mostafavi, M., Knowles, D., 2023. Grain size and shape dependent crystal plasticity finite element model and its application to electron beam welded SS316L. *J. Mech. Phys. Solids* 105331.
- Demir, E., Martinez-Pechero, A., Hardie, C., Tarleton, E., 2024. Restraining geometrically-necessary dislocations to the active slip systems in a crystal plasticity-based finite element framework. *Int. J. Plast.* 104013.
- Demir, E., Raabe, D., 2010. Mechanical and microstructural single-crystal bauschinger effects: Observation of reversible plasticity in copper during bending. *Acta Mater.* 58 (18), 6055–6063.
- Dunne, F., Rugg, D., Walker, A., 2007. Lengthscale-dependent, elastically anisotropic, physically-based hcp crystal plasticity: Application to cold-dwell fatigue in ti alloys. *Int. J. Plast.* 23 (6), 1061–1083.
- Follansbee, P., Kocks, U., 1988. A constitutive description of the deformation of copper based on the use of the mechanical threshold stress as an internal state variable. *Acta Metall.* 36 (1), 81–93.
- Gottstein, G., 2004. Physical foundations of materials science, vol. 3. Springer.
- Gu, X., Zhang, Q., Madenci, E., 2019. Non-ordinary state-based peridynamic simulation of elastoplastic deformation and dynamic cracking of polycrystal. *Eng. Fract. Mech.* 218, 106568.
- Hardie, C., Long, D.J., Demir, E., Tarleton, E., Dunne, F.P., 2023. A robust and efficient hybrid solver for crystal plasticity. *Int. J. Plast.* 170, 103773.
- Hardie, C., Thomas, R., Liu, Y., Frankel, P., Dunne, F., 2022. Simulation of crystal plasticity in irradiated metals: A case study on zircaloy-4. *Acta Mater.* 241, 118361.
- Harewood, F., McHugh, P., 2007. Comparison of the implicit and explicit finite element methods using crystal plasticity. *Comput. Mater. Sci.* 39 (2), 481–494.
- Hill, R., Rice, J., 1972a. Constitutive analysis of elastic-plastic crystals at arbitrary strain. *J. Mech. Phys. Solids* 20 (6), 401–413.
- Hill, R., Rice, J., 1972b. Constitutive analysis of elastic-plastic crystals at arbitrary strain. *J. Mech. Phys. Solids* 20 (6), 401–413.
- Hu, P., Liu, Y., Zhu, Y., Ying, L., 2016. Crystal plasticity extended models based on thermal mechanism and damage functions: Application to multiscale modeling of aluminum alloy tensile behavior. *Int. J. Plast.* 86, 1–25.
- Huang, Y., 1991. A user-material subroutine incorporating single crystal plasticity in the ABAQUS finite element program. Harvard Univ. Cambridge, UK.
- Jin, T., Mourad, H.M., Bronkhorst, C.A., Beyerlein, I.J., 2019. A single crystal plasticity finite element formulation with embedded deformation twins. *J. Mech. Phys. Solids* 133, 103723.
- Kabel, M., Fliegner, S., Schneider, M., 2016. Mixed boundary conditions for FFT-based homogenization at finite strains. *Comput. Mech.* 57, 193–210.
- Kalidindi, S., Anand, L., 1993. Large deformation simple compression of a copper single crystal. *Metallur. Trans. A* 24, 989–992.
- Kalidindi, S.R., Bronkhorst, C.A., Anand, L., 1992. Crystallographic texture evolution in bulk deformation processing of FCC metals. *J. Mech. Phys. Solids* 40 (3), 537–569.
- Kanit, T., Forest, S., Galliet, I., Mounoury, V., Jeulin, D., 2003. Determination of the size of the representative volume element for random composites: statistical and numerical approach. *International Journal of solids and structures* 40 (13–14), 3647–3679.
- Kapoor, K., Yoo, Y.S.J., Book, T.A., Kacher, J.P., Sangid, M.D., 2018. Incorporating grain-level residual stresses and validating a crystal plasticity model of a two-phase Ti-6Al-4 V alloy produced via additive manufacturing. *J. Mech. Phys. Solids* 121, 447–462.
- Khan, A.S., Huang, S., 1995. Continuum theory of plasticity. John Wiley & Sons.
- Knezevic, M., Drach, B., Ardeljan, M., Beyerlein, I.J., 2014. Three dimensional predictions of grain scale plasticity and grain boundaries using crystal plasticity finite element models. *Comput. Methods Appl. Mech. Engrg.* 277, 239–259.
- Knezevic, M., Zecevic, M., Beyerlein, I.J., Lebensohn, R.A., 2016. A numerical procedure enabling accurate descriptions of strain rate-sensitive flow of polycrystals within crystal visco-plasticity theory. *Comput. Methods Appl. Mech. Engrg.* 308, 468–482. <http://dx.doi.org/10.1016/j.cma.2016.05.025>.
- Kocks, U.F., Mecking, H., 2003. Physics and phenomenology of strain hardening: the fcc case. *Prog. Mater. Sci.* 48, 171–273.
- Lebensohn, R.A., 2001. N-site modeling of a 3D viscoplastic polycrystal using fast Fourier transform. *Acta Mater.* 49 (14), 2723–2737. [http://dx.doi.org/10.1016/S1359-6454\(01\)00172-0](http://dx.doi.org/10.1016/S1359-6454(01)00172-0).
- Lee, E.H., 1969. Elastic-plastic deformation at finite strains. *J. Appl. Mech.* 36 (1), 1–6. <http://dx.doi.org/10.1115/1.3564580>.
- Lieou, C.K., Bronkhorst, C.A., 2020. Thermodynamic theory of crystal plasticity: formulation and application to polycrystal fcc copper. *J. Mech. Phys. Solids* 138, 103905.
- Lim, H., Battaile, C.C., Bishop, J.E., Foulk, III, J.W., 2019. Investigating mesh sensitivity and polycrystalline RVEs in crystal plasticity finite element simulations. *Int. J. Plast.* 121, 101–115.
- Lindsay, A.D., Gaston, D.R., Permann, C.J., Miller, J.M., Andrš, D., Slaughter, A.E., Kong, F., Hansel, J., Carlsen, R.W., Icenhour, C., Harbour, L., Giudicelli, G.L., Stogner, R.H., German, P., Badger, J., Biswas, S., Chapuis, L., Green, C., Hales, J., Hu, T., Jiang, W., Jung, Y.S., Matthews, C., Miao, Y., Novak, A., Peterson, J.W., Prince, Z.M., Rovinelli, A., Schunert, S., Schwen, D., Spencer, B.W., Veeraraghavan, S., Recuero, A., Yushu, D., Wang, Y., Wilkins, A., Wong, C., 2022. 2.0 - MOOSE: Enabling massively parallel multiphysics simulation. *SoftwareX* 20, 101202. <http://dx.doi.org/10.1016/j.softx.2022.101202>, URL <https://www.sciencedirect.com/science/article/pii/S2352711022001200>.
- Maniatty, A., Dawson, P., Lee, Y.-S., 1992. A time integration algorithm for elasto-viscoplastic cubic crystals applied to modelling polycrystalline deformation. *Internat. J. Numer. Methods Engrg.* 35 (8), 1565–1588.
- Mánik, T., Asadkandi, H., Holmedal, B., 2022. A robust algorithm for rate-independent crystal plasticity. *Comput. Methods Appl. Mech. Engrg.* 393, 114831.
- Marin, E., Dawson, P., 1998. On modelling the elasto-viscoplastic response of metals using polycrystal plasticity. *Comput. Methods Appl. Mech. Engrg.* 165 (1–4), 1–21.
- Miehe, C., Schröder, J., Schotte, J., 1999. Computational homogenization analysis in finite plasticity simulation of texture development in polycrystalline materials. *Comput. Methods Appl. Mech. Engrg.* 171 (3–4), 387–418.
- Musinski, W.D., McDowell, D.L., 2015. On the eigenstrain application of shot-peened residual stresses within a crystal plasticity framework: Application to Ni-base superalloy specimens. *Int. J. Mech. Sci.* 100, 195–208.
- Niehäuser, A., Mosler, J., 2023. Numerically efficient and robust interior-point algorithm for finite strain rate-independent crystal plasticity. *Comput. Methods Appl. Mech. Engrg.* 416, 116392.
- Peirce, D., Asaro, R., Needleman, A., 1982. An analysis of nonuniform and localized deformation in ductile single crystals. *Acta Metall.* 30 (6), 1087–1119.
- Pokharel, R., Patra, A., Brown, D.W., Clausen, B., Vogel, S.C., Gray III, G.T., 2019. An analysis of phase stresses in additively manufactured 304L stainless steel using neutron diffraction measurements and crystal plasticity finite element simulations. *Int. J. Plast.* 121, 201–217.
- Prüger, S., Kiefer, B., 2020. A comparative study of integration algorithms for finite single crystal (visco-) plasticity. *Int. J. Mech. Sci.* 180, 105740.

- Quey, R., Dawson, P., Barbe, F., 2011. Large-scale 3D random polycrystals for the finite element method: Generation, meshing and remeshing. *Comput. Methods Appl. Mech. Engrg.* 200 (17–20), 1729–1745.
- Roters, F., Diehl, M., Shanthraj, P., Eisenlohr, P., Reuber, C., Wong, S.L., Maiti, T., Ebrahimi, A., Hochrainer, T., Fabritius, H.-O., et al., 2019. DAMASK—the Düsseldorf advanced material simulation kit for modeling multi-physics crystal plasticity, thermal, and damage phenomena from the single crystal up to the component scale. *Comput. Mater. Sci.* 158, 420–478.
- Roters, F., Eisenlohr, P., Kords, C., Tjahjanto, D.D., Diehl, M., Raabe, D., 2012. DAMASK: the düsseldorf advanced material simulation kit for studying crystal plasticity using an FE based or a spectral numerical solver. *Procedia Iutam* 3, 3–10.
- Roters, F., Raabe, D., Gottstein, G., 2000. Work hardening in heterogeneous alloys—a microstructural approach based on three internal state variables. *Acta Mater.* 48 (17), 4181–4189.
- Sarma, G., Zacharia, T., 1999. Integration algorithm for modeling the elasto-viscoplastic response of polycrystalline materials. *J. Mech. Phys. Solids* 47 (6), 1219–1238.
- Silling, S.A., Epton, M., Weckner, O., Xu, J., Askari, E., 2007. Peridynamic states and constitutive modeling. *J. Elasticity* 88, 151–184.
- Skamniotis, C., Grilli, N., Cocks, A.C., 2023. Crystal plasticity analysis of fatigue-creep behavior at cooling holes in single crystal nickel based gas turbine blade components. *Int. J. Plast.* 166, 103589.
- Sleeswyk, A., James, M., Plantinga, D., Maathuis, W., 1978. Reversible strain in cyclic plastic deformation. *Acta Metall.* 26 (8), 1265–1271.
- Sowerby, R., Uko, D., Tomita, Y., 1979. A review of certain aspects of the bauschinger effect in metals. *Mater. Sci. Eng.* 41 (1), 43–58.
- Sun, S., Sundararaghavan, V., 2014. A peridynamic implementation of crystal plasticity. *Int. J. Solids Struct.* 51 (19–20), 3350–3360.
- Takeuchi, T., 1975. Work hardening of copper single crystals with multiple glide orientations. *Trans. Japan Inst. Met.* 16 (10), 629–640.
- Tallman, A.E., Swiler, L.P., Wang, Y., McDowell, D.L., 2020. Uncertainty propagation in reduced order models based on crystal plasticity. *Comput. Methods Appl. Mech. Engrg.* 365, 113009.
- Tarleton, E., 2023. Github link for crystal plasticity code. <https://github.com/TarletonGroup/CrystalPlasticity> (Accessed: 30 September 2024).
- Veasna, K., Feng, Z., Zhang, Q., Knezevic, M., 2023. Machine learning-based multi-objective optimization for efficient identification of crystal plasticity model parameters. *Comput. Methods Appl. Mech. Engrg.* 403, 115740.
- Wagoner, R., 1980. Measurement and analysis of plane-strain work hardening. *Metall. Mater. Trans. A* 11, 165–175.
- Weber, G., Anand, L., 1990. Finite deformation constitutive equations and a time integration procedure for isotropic, hyperelastic-viscoplastic solids. *Comput. Methods Appl. Mech. Engrg.* 79 (2), 173–202.
- Weber, G., Pinz, M., Ghosh, S., 2022. Machine learning-enabled self-consistent parametrically-upscaled crystal plasticity model for Ni-based superalloys. *Comput. Methods Appl. Mech. Engrg.* 402, 115384.
- Zhang, M., Nguyen, K., Segurado, J., Montans, F.J., 2021. A multiplicative finite strain crystal plasticity formulation based on additive elastic corrector rates: Theory and numerical implementation. *Int. J. Plast.* 137, 102899.